

Breakdown of Quantum Chaos in the Staggered-Field XXZ Chain: Confinement and Meson Formation

Julia Wildeboer,^{1,2} Marton Lajer,¹ and Robert M. Konik¹

¹*Division of Condensed Matter Physics and Materials Science,
Brookhaven National Laboratory, Upton, NY 11973-5000, USA*

²*Perimeter Institute for Theoretical Physics, Waterloo, Ontario, N2L 2Y5, Canada*

Confinement of fractionalized excitations can strongly restructure many-body spectra. We investigate this phenomenon in the gapped spin- $\frac{1}{2}$ XXZ chain subject to a staggered field, where spinons bind into domain-wall “mesons” deep in the antiferromagnetic phase. We present evidence that this non-integrable model exhibits both Hilbert space fractionalization and quantum scar formation as controlled by the anisotropy parameter Δ . Exact diagonalization across symmetry-resolved sectors reveals a crossover from Gaussian-orthogonal (chaotic) level statistics at weak anisotropy $\Delta \sim 1$ to non-ergodic behavior deep in the antiferromagnetic regime $\Delta \gg 1$ through scrutinizing the adjacent gap ratios, accompanied by a striking banding of eigenstates by domain-wall number in correlation and entanglement measures. The Page-like entanglement dome characteristic of chaotic spectra gives way to suppressed, band-resolved entanglement consistent with emergent quasi-conservation of domain walls. To investigate further the formation mechanism of mesonic scar states, we carry out meson spectroscopy near the two-spinon threshold and compare with the analytic ladder predicted by Rutkevich [Phys. Rev. B 106, 134405 (2022)]. We test the theory through continuum-relative bindings, an offset-removed Airy scaling collapse, and explicit two-meson thresholds that determine the number of stable meson levels. The low-lying spectrum shows close quantitative agreement, while deviations at higher energies are consistent with finite-size and subleading corrections. These results establish a unified account of confinement-induced nonergodicity and provide a template for quantitative meson spectroscopy in quantum spin chains.

I. INTRODUCTION

A central question in non-equilibrium many-body physics is how and when highly excited eigenstates depart from the eigenstate thermalization hypothesis (ETH) [1, 2]. While the ETH explains why generic interacting systems thermalize, several robust mechanisms are now known to violate it even in the absence of quenched disorder. Examples include many-body localization [3, 4], kinetic constraints, and more recently, the phenomena of Hilbert-space fragmentation and quantum many-body scars [5–14]. These distinct mechanisms give rise to nonergodic dynamics in otherwise translationally invariant systems.

Hilbert-space fragmentation occurs when exact or emergent conservation laws divide the Hilbert space into dynamically disconnected or weakly coupled subsectors, thereby preventing complete thermalization. In its strong form, as realized, for example, in dipole-conserving or fracton-like Hamiltonians, dynamics remain confined within independent fragments while in its weak form, approximate conservation laws produce long-lived subspaces that eventually thermalize but only on very long timescales [5, 7, 8]. Quantum many-body scars, by contrast, correspond to special low-entanglement eigenstates embedded within a continuum of thermal ones, leading to coherent oscillations and slow relaxation from particular initial conditions [15–23]. Together, these two ideas capture much of the current theoretical landscape of disorder-free nonergodicity [12, 14].

A complementary, and physically transparent, route to ergodicity breaking arises from confinement. When local interactions generate a linear potential between fractionalized excitations, these excitations become bound into composite objects, i.e., “mesons” that can no longer freely propagate. This confinement suppresses the mixing of local degrees of

freedom and thereby hinders thermalization [24–28]. In this sense, confinement can be viewed as a natural, dynamical realization of *weak Hilbert-space fragmentation*, producing long-lived, structured eigenstates without fine-tuning or disorder [27].

The paradigmatic realization of confinement in one dimension is the Ising chain in a longitudinal field, where spinons experience a linear potential and form bound states that manifest as a “meson ladder.” Recent theoretical work and cold-atom experiments have shown that such confined systems display slow relaxation, nonthermal eigenstate statistics, and characteristic entanglement features reflecting their composite excitations [25, 26, 28, 29]. Motivated by these results, it is natural to ask whether similar confinement-induced signatures appear in other one-dimensional models of correlated spins.

In this paper we study the spin- $\frac{1}{2}$ XXZ chain in a staggered magnetic field, which is a minimal, clean, and well-controlled system that exhibits all essential ingredients of confinement-induced ETH breakdown. Turning on a staggered field breaks one-site translation while preserving two-site translational symmetry, creating alternating local environments that generate a linear confining potential between domain walls. The resulting bound states are mesons that can be labeled by an emergent domain-wall number W , which behaves as a quasi-conserved quantity. This provides a microscopic route to weak fragmentation in a physically realistic model.

The staggered-field XXZ chain thus serves as an archetype for understanding how simple, local interactions can produce nonergodic spectra through confinement. Its behavior also connects directly to other disorder-free mechanisms of ETH violation. In constrained dipole-conserving models, strong versus weak fragmentation have been distinguished depending on whether exact higher-moment conservation strictly sec-

torizes dynamics or whether small symmetry-breaking perturbations eventually restore ergodicity while leaving long-lived subspaces [5, 7]. Analogously, the approximate conservation of the number of domain-walls W in our model dynamically generates a weakly fragmented Hilbert-space structure.

This picture naturally relates to the study of quantum many-body scars, where certain low-entanglement eigenstates coexist with an otherwise chaotic spectrum. Scarred dynamics have been observed in the PXP model relevant for Rydberg-atom chains, as well as in the Affleck–Kennedy–Lieb–Tasaki (AKLT) model and its deformations [15, 17–22, 30–32]. The AKLT chain provides a paradigmatic example since its exact matrix-product ground state and tower of quasiparticle excitations form a protected, nonthermal subspace within a local Hamiltonian [30, 31]. Recent studies of deformed AKLT-type and spin-1 XY models have revealed families of scarred excitations and weakly fragmented dynamics [22, 32].

Our staggered-field XXZ model complements these developments from a different angle. Instead of algebraically protected subspaces, here nonergodic behavior emerges dynamically from confinement, i.e. a purely energetic constraint that organizes the spectrum into meson bands and reduces entanglement within each band. This demonstrates that fragmentation-like and scar-like structures can emerge naturally from generic microscopic mechanisms such as confinement, providing a bridge between exactly solvable and physically realistic models.

Moreover, confinement is not merely a theoretical construct. Signatures of confined bound states have been experimentally observed in a variety of quasi-one-dimensional quantum magnets, such as YbAlO_3 , Cs_2CoCl_4 , and the $\text{Ba}(\text{Sr})\text{Co}_2\text{V}_2\text{O}_8$ family, where an effective staggered field produced by weak interchain couplings leads to the formation of Zeeman ladders seen in inelastic neutron scattering [33–45]. These materials thus provide realistic experimental platforms for exploring the interplay between confinement, fragmentation, and nonergodicity.

With these motivations, we establish the staggered-field

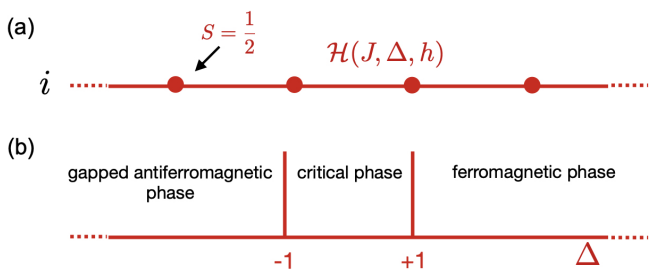


FIG. 1. *The spin- $\frac{1}{2}$ XXZ spin chain and its zero field phase diagram.* (a) A one-dimensional chain of $S = \frac{1}{2}$ spins that interact via couplings J and Δ in the presence of a staggered magnetic field. (b) At zero staggered magnetic field ($h = 0$) the Hamiltonian $\mathcal{H}(J, \Delta, 0)$ realizes three distinct phases depending on the anisotropy parameter Δ : the ferromagnetic phase at $\Delta > 1$, the critical phase at $-1 < \Delta < 1$, and the gapped antiferromagnetic (AF) phase at $\Delta < -1$. The candidate region for the occurrence of scar-like meson states is the gapped AF phase.

XXZ chain as a quantitative and conceptually transparent setting where confinement, Hilbert-space fragmentation, and scar-like behavior intersect. We show that confinement produces a clear crossover from chaotic (GOE) to nonergodic (Poisson-like) level statistics, banded structures in spin correlations and entanglement entropy linked to W , and an analytic meson ladder that matches exact diagonalization (ED) quantitatively. The model therefore unifies global and local diagnostics of nonergodicity within a single, microscopically tractable Hamiltonian.

Our central findings on the XXZ model tie together four complementary diagnostics. (i) *Level statistics.* We observe a crossover from Gaussian-orthogonal-ensemble (GOE) behavior at weak anisotropy to nonergodic, Poisson-like statistics deep in the antiferromagnetic (AF) regime, with the finite-size drift of the adjacent-gap ratio pointing toward a thermodynamic scale where confinement dominates spectral correlations. (ii) *Correlation banding.* A simple nearest-neighbor correlator C_j^{zz} (referenced to the ground state) reveals flat “bands” of eigenstates that are approximately labeled by a domain-wall number W . (iii) *Entanglement reorganization.* The bipartite von Neumann entropy S^{vN} exhibits the familiar ETH “dome” at small anisotropy $|\Delta|$, peaking near the random-state (Page) value. As $|\Delta|$ increases and confinement strengthens, the entanglement S^{vN} splits into sub-Page bands mirroring the behavior seen in specific correlations. (iv) *Quantitative meson spectroscopy.* We compare an analytical meson ladder to numerical ED results and find good agreement in the weak staggered field regime.

Conceptually, this unifies global and local diagnostics in the form of level statistics and entanglement/correlations, respectively, with controlled analytics in a single lattice model. While our focus is on confinement, the connection to “scar-like” phenomenology is instructive. The meson bands furnish atypical, low-entanglement eigenstates embedded in a sea of chaotic states, and they can exhibit slow relaxation from specially prepared initial states—features reminiscent of quantum many-body scars [15–23]. The key distinction is origin and scope. The nonergodic structure follows from a generic binding mechanism rather than from an exact embedded tower, suggesting greater robustness and clearer materials relevance.

The remainder of this work is structured as follows. Section II introduces the staggered-field XXZ model and its symmetries. Section III presents level statistics and the chaos–nonergodicity crossover. The subsequent Sections IV and V on correlations and on eigenstate entanglement detail the emergence of banded structure in correlations and in entanglement entropy measurements connected to the emergence of mesons, respectively. Section VI develops the analytic meson spectrum and compares it quantitatively to ED, while Section VII concludes with an outlook and implications for future experiments.

II. XXZ SPIN CHAIN MODELS

Motivated by the search for long-lived nonergodic excitations in realistic materials (e.g., rare-earth spin-chain com-

symmetry	symbol	quantum number	action/description
U(1) spin (about z)	S_{tot}^z	S_{tot}^z	total magnetization $S_{\text{tot}}^z = \sum_{i=1}^N \sigma_i^z$ is conserved
two-site translation	\mathcal{T}_2	P_n	$i \mapsto i + 2$; momenta $P_n = 4\pi n/N$, $n = 0, \dots, \frac{N}{2} - 1$
inversion (parity)	\mathcal{I}	$I = \pm 1$	site reflection: $i \mapsto N + 1 - i$
staggered spin-flip	$\mathcal{C}_{\text{flip}} = \mathcal{T}_1 \prod_i \sigma_i^x$	$C_f = \pm 1$	one-site translation composed with global spin flip

TABLE I. *Symmetries of the XXZ chain with a staggered field with periodic boundary conditions (PBCs).* The one-site translation is broken by the staggered field, but a two-site translation \mathcal{T}_2 survives, leading to momenta quantized in units of $4\pi/N$. The inversion \mathcal{I} reflects the chain about its center, i.e. $i \mapsto N + 1 - i$. The operation $\mathcal{C}_{\text{flip}}$ compensates the sign change of the staggered field under \mathcal{T}_1 via a global spin flip; it squares to \mathcal{T}_2 (nonsymmorphic structure) and partitions each \mathcal{T}_2 momentum sector into $C_f = \pm 1$ subsectors.

pounds such as YbAlO_3), we study the spin- $\frac{1}{2}$ XXZ chain subject to a staggered magnetic field. Our focus throughout is the antiferromagnetic Ising regime where confined domain-wall bound states (“mesons”) emerge.

A. XXZ chain in a staggered magnetic field

We consider the periodic spin chain described by the Hamiltonian

$$\begin{aligned} \mathcal{H}(J, \Delta, h) = & -J \sum_{i=1}^N \left(\sigma_i^x \sigma_{i+1}^x + \sigma_i^y \sigma_{i+1}^y + \Delta \sigma_i^z \sigma_{i+1}^z \right) \\ & - h \sum_{i=1}^N (-1)^i \sigma_i^z \end{aligned} \quad (2.1)$$

with $J > 0$, Pauli matrices σ_i^α , ($\alpha = x, y, z$) on site i , anisotropy Δ , and staggered-field strength h . We assume periodic boundary conditions (PBC), i.e. $\sigma_{N+1}^\alpha \equiv \sigma_1^\alpha$.

At zero staggered field h the model (2.1) exhibits three standard phases as Δ is varied: (i) a ferromagnetic Ising phase for $\Delta > 1$, (ii) a critical (Luttinger-liquid) phase for $-1 < \Delta < +1$, and (iii) a gapped antiferromagnetic Ising phase for $\Delta < -1$ [see Fig. 1(a) and (b)]. Note that the overall minus sign in (2.1) is our convention. With $J > 0$ this places the AF Ising regime at $\Delta < -1$. Turning on the staggered field ($h \neq 0$) breaks the one-site translation symmetry and, in the Ising regime, confines spinons into mesonic bound states that are scar-like states.

B. Symmetries of the spin chain Hamiltonian $\mathcal{H}(J, \Delta, h)$

The model (2.1) retains four useful, distinctive symmetries (see Table I). First there is an U(1) symmetry about the z -axis, i.e. the z -component of the spin is conserved since the Hamiltonian commutes with the total z -magnetization operator $S_{\text{total}}^z = \sum_i \sigma_i^z$ due to the absence of terms that mix x, y and z components asymmetrically. Further there is a reduced two-site translational symmetry \mathcal{T}_2 since the Hamiltonian is invariant under translations by two sites but not under translations by one site due to the staggered magnetic field. Moreover, we observe a spatial inversion symmetry, i.e. the Hamiltonian is symmetric under spatial inversion, i.e.

$i \mapsto N - i + 1$, as both the interaction term and the alternating field respect inversion symmetry. The list is completed by a nonsymmorphic \mathcal{Z}_2 symmetry in form of a combined translation by one site and a global spin flip given by $\mathcal{C}_{\text{flip}} = \mathcal{T}_1 \prod_i \sigma_i^x$. For reference, the size of the Hilbert-space block selected by $(S_{\text{total}}^z, P, \mathcal{I}, \mathcal{C}_{\text{flip}}) = (0, 0, +1, +1)$ as a function of N is listed in Table II where the last column shows the fraction of the $S_{\text{total}}^z = 0$ sector retained after projecting onto $(P, \mathcal{I}, \mathcal{C}_{\text{flip}}) = (0, +1, +1)$.

III. LEVEL STATISTICS AND CROSSOVER TO NONERGODIC BEHAVIOR

To characterize the spectral properties of the spin- $\frac{1}{2}$ XXZ chain in a staggered magnetic field [Eq. (2.1)], we start by analyzing the level statistics of its many-body energy spectrum. The energy eigenvalues E_n are ordered in ascending order and restricted to the fixed symmetry sector $(S_{\text{total}}^z, P, \mathcal{I}, \mathcal{C}_{\text{flip}}) = (0, 0, +1, +1)$. Throughout this section we analyze spectra in the fixed $(S_{\text{total}}^z, P, \mathcal{I}, \mathcal{C}_{\text{flip}}) = (0, 0, +1, +1)$ block. The corresponding block dimensions for $N = 4, \dots, 22$ are compiled in Table II.

For each consecutive triplet of energy levels (E_n, E_{n+1}, E_{n+2}) , we define the ratio of adjacent spac-

N	$\dim \mathcal{H}(S_{\text{tot}}^z=0) = \binom{N}{N/2}$	$\dim \mathcal{H}_{\text{sub}}$	$\dim \mathcal{H}_{\text{sub}} / \binom{N}{N/2}$
4	6	3	0.50
6	20	6	0.30
8	70	11	0.157
10	252	26	0.103
12	924	62	0.0671
14	3432	170	0.0495
16	12870	487	0.0379
18	48620	1530	0.0315
20	184756	4947	0.0268
22	705432	16718	0.0237

TABLE II. Block dimensions for the XXZ chain (PBC) in the symmetry sector $(S_{\text{tot}}^z, P, \mathcal{I}, \mathcal{C}_{\text{flip}}) = (0, 0, +1, +1)$. The second column lists the size of the $S_{\text{tot}}^z=0$ block, and the last column shows the fraction kept after projecting to $(P, \mathcal{I}, \mathcal{C}_{\text{flip}}) = (0, +1, +1)$.

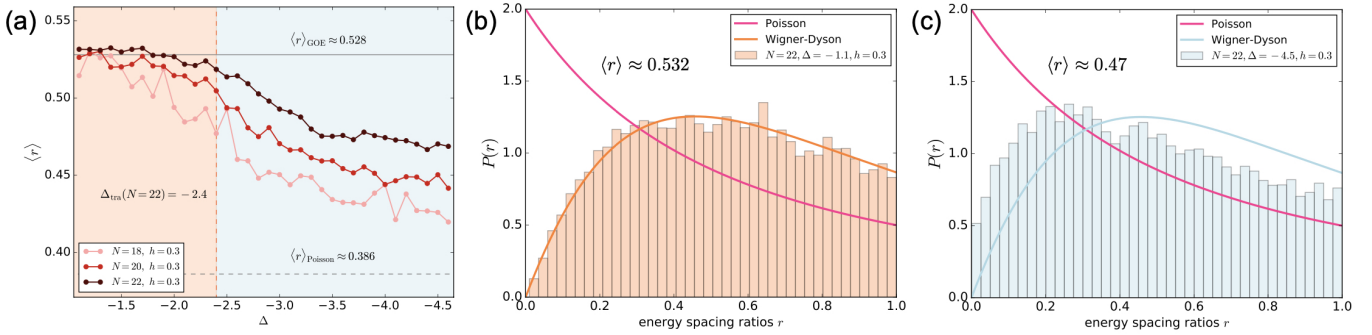


FIG. 2. Average level-spacing ratio $\langle r \rangle$ versus anisotropy Δ for the spin- $\frac{1}{2}$ XXZ chain $\mathcal{H}(1, \Delta, h)$ in a staggered magnetic field h , resolved in the symmetry sector with $(S_{\text{total}}^z, P, \mathcal{I}, \mathcal{C}_{\text{flip}}) = (0, 0, +1, +1)$. (a) Average adjacent gap ratio $\langle r \rangle$ as a function of anisotropy Δ for chain lengths $N = 18, 20, 22$ at $h = 0.3$. The horizontal lines indicate the Gaussian orthogonal ensemble (GOE) value $\langle r \rangle_{\text{GOE}} \approx 0.528$ and the Poisson value $\langle r \rangle_{\text{Poisson}} \approx 0.386$. For $N = 22$ we observe that for $\Delta \gtrsim -2.3$ (orange region), $\langle r \rangle$ approaches the GOE prediction, consistent with quantum chaotic behavior, while for $\Delta \lesssim -2.3$ (blue region), $\langle r \rangle$ decreases, signaling a crossover towards nonergodic behavior. (b) Distribution $P(r)$ of the energy level spacing ratios r for $N = 22, \Delta = -1.1$, and $h = 0.3$. The histogram is compared to the Poisson (magenta) and Wigner-Dyson (orange) distributions, with $\langle r \rangle \approx 0.532$ indicating spectral statistics close to GOE. (c) Same as (b) but for $\Delta = -4.5$, deep in the antiferromagnetic phase. Here $P(r)$ deviates from Wigner-Dyson statistics and shifts towards Poisson-like behavior, with $\langle r \rangle \approx 0.47$, reflecting the onset of spectral clustering and emergent integrability associated with quasi-conserved quantities in the confined phase.

ings as

$$r_n = \frac{\min(E_{n+1} - E_n, E_{n+2} - E_{n+1})}{\max(E_{n+1} - E_n, E_{n+2} - E_{n+1})}. \quad (3.1)$$

We then compute the mean level-spacing ratio

$$\langle r \rangle = \langle r_n \rangle, \quad (3.2)$$

where the average is taken over all eigenstates in the symmetry sector.

Random matrix theory predicts distinct universal values of $\langle r \rangle$ for chaotic versus integrable spectra [46, 47], i.e. for Gaussian orthogonal ensemble (GOE) statistics, $\langle r \rangle_{\text{GOE}} \approx 0.536$ and for uncorrelated (Poisson) statistics characteristic of integrable or many-body localized systems we have $\langle r \rangle_{\text{Poisson}} \approx 0.386$. Moreover we analyze the full probability distribution $P(r)$ of the ratios r_n to further characterize the spectral correlations.

Figure 2(a) shows the finite-size dependence of $\langle r \rangle$ as a function of the anisotropy factor Δ for system sizes $N =$

h	$\langle r \rangle (N=20)$	$\langle r \rangle (N=22)$
0.1	0.437191	0.443036
0.2	0.428236	0.472977
0.3	0.452605	0.496836
0.4	0.455710	0.500026
0.5	0.456062	0.505295

TABLE III. Mean adjacent-gap ratio $\langle r \rangle$ in the fixed domain-wall sector $W = 10$ for $\Delta = -4.5$ within the symmetry block $(S_{\text{total}}^z, P, \mathcal{I}, \mathcal{C}_{\text{flip}}) = (0, 0, +1, +1)$. Values are shown for chain lengths $N = 20$ and $N = 22$ as a function of the staggered field h . For reference, $\langle r \rangle_{\text{GOE}} \approx 0.536$ and $\langle r \rangle_{\text{Poisson}} \approx 0.386$. The $W=10$ subspace has dimension 1651 for $N = 20$ and 5419 for $N = 22$.

18, 20, 22 at $h = 0.3$. For Δ close to the isotropic point ($\Delta \gtrsim -1.5$), the level statistics is size-independent and agrees with the GOE prediction, reflecting fully developed quantum chaos. As Δ decreases below approximately -2 , $\langle r \rangle$ begins to fall below the GOE value, with the crossover point shifting to more negative Δ for larger N . This reduction in $\langle r \rangle$ signals a breakdown of chaotic behavior and the onset of nonergodic spectral statistics associated with the emergence of quasi-conserved quantities in the antiferromagnetic regime.

Panels (b) and (c) of Fig. 2 display the distributions $P(r)$ for two representative values of Δ . For $\Delta = -1.1$ [panel (b)], the histogram matches the Wigner-Dyson distribution characteristic of the GOE, with $\langle r \rangle \approx 0.532$. In contrast, for $\Delta = -4.5$ [panel (c)], $P(r)$ exhibits suppressed level repulsion and approaches a Poisson-like form, with $\langle r \rangle \approx 0.47$. The latter behavior reflects strong spectral clustering, consistent with the formation of nearly conserved domain-wall configurations and confined meson excitations.

To isolate the role of the domain-wall bands characterized by the number of domain walls $W = 2n$ with $n = 0, 1, \dots, N/2$, we further restricted the statistics to a fixed $W = 10$ subsector within the same symmetry block at $\Delta = -4.5$. Table III lists $\langle r \rangle$ versus h for $N = 20, 22$. In both sizes the values lie between Poisson and GOE, indicating partial level repulsion within a constrained manifold. For $N = 22$ the mean ratio drifts upward with h (from 0.443 at $h = 0.1$ to 0.505 at $h = 0.5$), consistent with enhanced hybridization within the $W = 10$ band as the staggered field increases. At $N = 20$ the variation is weaker and mildly nonmonotonic near $h=0.2$, plausibly a finite-size effect given the smaller subspace dimension (1651 vs. 5419 states). Overall, these fixed- W results support the picture that nonergodicity at large negative Δ is tied to emergent band structure in domain-wall number, with increasing h tending to restore level repulsion within a given band.

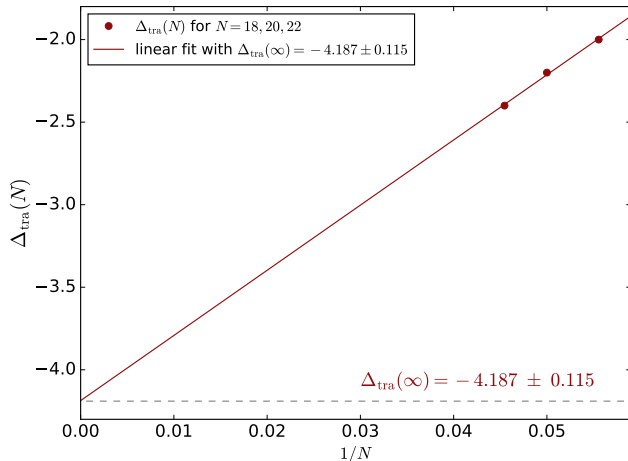


FIG. 3. Finite-size scaling of the transition anisotropy $\Delta_{\text{tra}}(N)$ for the spin- $\frac{1}{2}$ XXZ chain $\mathcal{H}(1, \Delta, h)$ in a staggered magnetic field $h = 0.3$, evaluated in the symmetry sector $(S_{\text{total}}^z, P, \mathcal{I}, C_{\text{flip}}) = (0, 0, +1, +1)$. The transition points $\Delta_{\text{tra}}(N)$ are extracted from the crossover in the average level-spacing ratio $\langle r \rangle$ for system sizes $N = 18, 20, 22$ [see Fig. 2(a)] and plotted as a function of $1/N$. The linear fit (solid line) extrapolates to $\Delta_{\text{tra}}(\infty) = -4.19 \pm 0.115$ in the thermodynamic limit, indicating the onset of nonergodic behavior and confinement deep in the antiferromagnetic phase.

To quantify the crossover, we extract the values $\Delta_{\text{tra}}(N)$ at which $\langle r \rangle$ begins to deviate from the GOE value for each system size N . These transition points, shown in Fig. 3 as a function of $1/N$, shift to more negative anisotropy with increasing N . A linear fit of $\Delta_{\text{tra}}(N)$ versus $1/N$ yields the thermodynamic estimate $\Delta_{\text{tra}}(\infty) \approx -4.19 \pm 0.115$. This value marks the onset of nonergodic behavior and confinement deep in the antiferromagnetic phase.

IV. CORRELATIONS IN THE SPIN CHAIN

To further characterize the properties of the staggered-field XXZ chain (2.1), we now turn to the study of correlation functions. These observables provide insight into the magnetic ordering of the system as well as the emergence of domain-wall excitations in different parameter regimes. For an eigenstate $|\psi\rangle$, we evaluate both local magnetization and nearest-neighbor spin correlations.

We first define the staggered longitudinal magnetization which captures the presence of antiferromagnetic order as

$$\langle \sigma^z \rangle_{\text{stag}} = \frac{1}{N} \sum_{i=1}^N (-1)^i \langle \psi | \sigma_i^z | \psi \rangle. \quad (4.1)$$

Here, σ_i^z is the Pauli z -operator on site i , and N is the total number of sites [48]. In addition, we analyze the average nearest-neighbor spin-spin correlation

$$\langle \sigma_i^z \sigma_{i+1}^z \rangle_{\text{av}} = \frac{1}{N} \sum_{i=1}^N \langle \psi | \sigma_i^z \sigma_{i+1}^z | \psi \rangle. \quad (4.2)$$

This quantity is directly related to the density of domain walls and provides a convenient probe for the degree of antiferromagnetic ordering in the system.

For large negative anisotropy Δ (deep in the antiferromagnetic regime), the number of domain walls is expected to become a quasi-conserved quantity. To test this hypothesis, we introduce the correlation measure

$$C_j^{zz}(|\psi_j\rangle, |\psi_0\rangle) = \langle \psi_j | \sum_i \sigma_i^z \sigma_{i+1}^z | \psi_j \rangle - \langle \psi_0 | \sum_i \sigma_i^z \sigma_{i+1}^z | \psi_0 \rangle \quad (4.3)$$

where $|\psi_j\rangle$ is an excited eigenstate and $|\psi_0\rangle$ is the ground state of the Hamiltonian (2.1). The quantity $C_j^{zz}(|\psi_j\rangle, |\psi_0\rangle)$ measures the deviation of nearest-neighbor spin correlations in $|\psi_j\rangle$ from those of the ground state and serves as an indicator of the domain-wall content of the excitation.

The behavior of these correlation functions across the many-body spectrum is shown in Figs. 4(a) and 5(a) for a chain of size $N = 20$ at several values of the anisotropy parameter Δ . Figure 4(a) displays the correlation measure C_j^{zz} versus the energy per site $E/N + E_{\text{shift}}$ [49] for different anisotropies $\Delta = -1.1, -2.6, -3.1, -4.5$. For weak anisotropy ($\Delta = -1.1$), the values of C_j^{zz} form a single broad distribution, indicating that domain-wall configurations are highly mobile and not associated with well-defined quantum numbers. As $|\Delta|$ increases, the spectrum develops a clear banded structure, where states cluster into branches with nearly constant C_j^{zz} . This banding becomes more pronounced for large negative anisotropy ($\Delta = -4.5$) as depicted in Figs. 4(a) and 5(a), consistent with the picture that the number of domain walls W becomes a quasi-conserved quantity in the deep antiferromagnetic phase.

Figure 4(b) shows the corresponding staggered magnetization $\langle \sigma_i^z \rangle_{\text{stag}}$ for the same parameters $\Delta = -1.1, -2.6, -3.1$. For small $|\Delta|$, the distribution of $\langle \sigma_i^z \rangle_{\text{stag}}$ remains narrow around zero, reflecting the absence of long-range antiferromagnetic order in the chaotic regime. For larger $|\Delta|$, the distribution becomes wider and structured, indicating enhanced antiferromagnetic correlations and a tendency toward domain-wall localization.

Finally, Fig. 5 focuses on the case $\Delta = -4.5$, deep inside the antiferromagnetic regime. Figure 5(a) shows that the eigenstates segregate into well-defined flat branches labeled by the number of domain walls $W = 2n$ with $n = 0, 2, \dots, N/2$, confirming that W acts as an emergent approximate quantum number whereas Fig. 5(b) shows that the staggered magnetization exhibits the same band structure, with each branch corresponding to a distinct domain-wall sector. Low-energy states with $W = 2$ correspond to meson-like excitations with strong antiferromagnetic correlations, while higher W sectors exhibit progressively smaller staggered magnetization.

In summary, the correlation analysis reveals a crossover from a chaotic regime at small $|\Delta|$, where domain walls are highly mobile and no clear structure is visible, to a nonergodic regime at large negative Δ , where the number of domain walls becomes quasi-conserved, the spectrum organizes into bands,

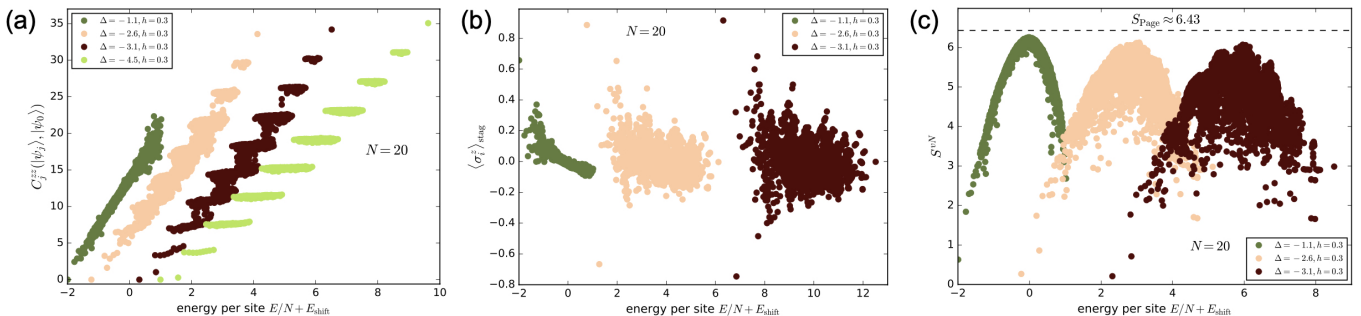


FIG. 4. *Correlation measure, staggered magnetization, and entanglement entropy across the spectrum of the staggered-field XXZ chain.* (a) Correlation measure $C_j^{zz}(|\psi_j\rangle, |\psi_0\rangle)$ vs. energy per site $E/N + E_{\text{shift}}$ for $N = 20$, $h = 0.3$, and anisotropies $\Delta = -1.1, -2.6, -3.1, -4.5$ with respective energy shift $E_{\text{shift}} = 0.0, 2.0, 4.0, 6.0$. For small $|\Delta|$, C_j^{zz} forms a single broad cloud while for larger $|\Delta|$ the spectrum splits into distinct branches associated with different domain-wall numbers W (banding). (b) Staggered magnetization $\langle \sigma_i^z \rangle_{\text{stag}}$ for the same system, which remains small and disordered at weak anisotropy and becomes structured as $|\Delta|$ grows, consistent with strengthening antiferromagnetic correlations. (c) Von Neumann entanglement S^{vN} for the same parameters. At small $|\Delta|$, S^{vN} exhibits a volume-law “dome” consistent with quantum chaos while for larger $|\Delta|$, clear bands of reduced entropy emerge, signaling the onset confinement and nonergodicity [also see Fig. 5(c)]. A dashed horizontal line marks the Page benchmark for a half chain ($N_A = N_B = 10$) entanglement entropy of $S_{\text{Page}} = 10 \ln(2) - \frac{1}{2} \approx 6.43$.

and meson-like bound states emerge. These findings complement the level statistics results and provide microscopic insight into the confinement mechanism in the staggered-field XXZ chain.

V. EIGENSTATE ENTANGLEMENT ACROSS THE SPECTRUM

Entanglement measures provide a powerful framework to characterize the structure of many-body eigenstates and to distinguish between different dynamical regimes. Unlike conventional correlation functions, which probe specific local observables, entanglement quantifies the global quantum correlations encoded in a wave function. This makes it an especially sensitive probe for detecting the crossover from chaotic to nonergodic behavior in interacting quantum systems. We quantify it via the bipartite von Neumann entropy

$$S^{\text{vN}} = -\text{Tr}(\rho_A \ln \rho_A), \quad (5.1)$$

where the system is partitioned into contiguous regions A and B such that the Hilbert space factorizes as $\mathcal{H} = \mathcal{H}_A \otimes \mathcal{H}_B$ and the reduced density matrix of region A is $\rho_A = \text{Tr}_B |\psi\rangle\langle\psi|$ obtained by tracing out the degrees of freedom in region B . Throughout we use natural logarithms and evaluate S^{vN} for half-chain cuts ($N_A = N_B = N/2$) for all eigenstates $|\psi\rangle$ of the staggered-field XXZ Hamiltonian (2.1), analyzing its dependence on anisotropy Δ and energy density E/N .

As a benchmark for chaotic eigenstates we use the random-state (Page) average for a bipartition with $N_A \leq N_B$,

$$S_{\text{Page}} = N_A \ln(2) - \frac{2^{N_A}}{2^{N_B+1}} + O(2^{-2N_B}). \quad (5.2)$$

In our half-chain geometry with $N = 20$ ($N_A = N_B = 10$), this yields

$$S_{\text{Page}} = 10 \ln(2) - \frac{1}{2} \approx 6.43, \quad (5.3)$$

which we use as a reference for mid-spectrum states [indicated by a dashed line in Figs. 4(c) and 5(c)]. The behavior of the entanglement entropy across the many-body spectrum is shown in Figs. 4(c) and 5(c) for $\Delta = -1.1, -2.6, -3.1$ and -4.5 , respectively. For small $|\Delta|$, plotting S^{vN} versus energy density $E/N + E_{\text{shift}}$ produces the familiar broad, nearly symmetric ETH “dome”: entanglement is suppressed in the spectral tails and peaks near mid-spectrum, clustering around S_{Page} as seen in Fig. 4(c). By contrast, nonergodic or localized eigenstates exhibit substantially reduced entanglement that tends toward area-law scaling. Thus, persistent sub-Page values and departures from the dome serve as a simple diagnostic.

Upon increasing $|\Delta|$ into the antiferromagnetic Ising regime, the distribution of S^{vN} is globally reduced and develops visible structure across the spectrum [Figs. 4(c) and 5(c)]. The reorganization mirrors the band formation seen in correlation diagnostics. The correlation measure $C_j^{zz}(|\psi_j\rangle, |\psi_0\rangle)$ (4.3) plotted versus the energy per site E/N clusters eigenstates $|\psi\rangle$ into nearly flat branches that are approximately labeled by the domain-wall number W [see Fig. 5(a)]. Deep in the AF regime ($\Delta = -4.5$) this banding becomes sharp and is reflected one-to-one in S^{vN} . The one-meson band ($W = 2$), i.e. member states consist of two aligned bonds (two kinks) independent of energy, sits at $C_j^{zz}(|\psi\rangle, |\psi\rangle) \simeq +4$ and exhibits distinctly low entanglement compared to the chaotic background while higher- W branches appear near $+8, +12, \dots$ with progressively larger, yet still sub-Page, entanglement [Fig. 5(c)]. This clear correspondence between the correlation measure and the entanglement entropy supports the interpretation that domain-wall number is a quasi-conserved quantity in the deep antiferromagnetic phase. Contrarily, as discussed previously, for small $|\Delta|$ (e.g. $\Delta = -1.1$), the spectrum forms a broad cloud without clear separation, reflecting fully chaotic dynamics and delocalized domain walls.

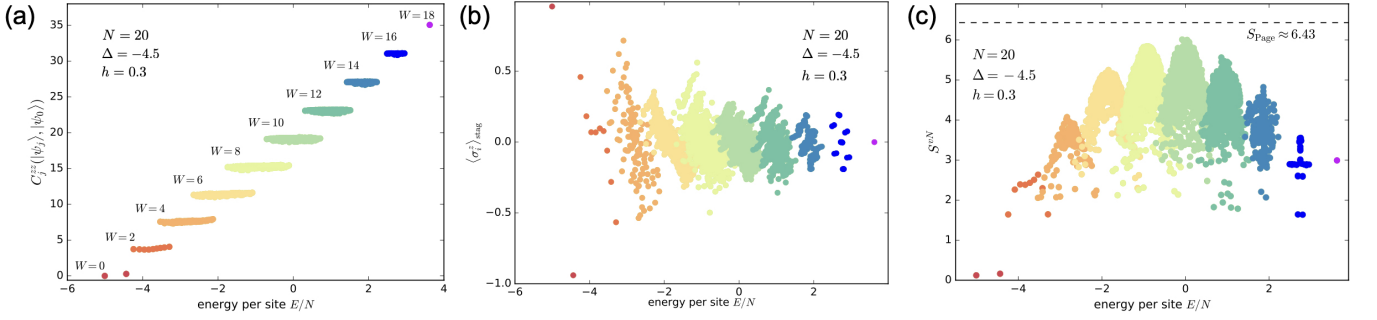


FIG. 5. *Banded structure at strong anisotropy* ($\Delta = -4.5$) and its entanglement signature. (a) Correlation measure $C_j^{zz}(|\psi_j\rangle, |\psi_0\rangle)$ versus energy per site E/N for eigenstates of the $N = 20$ chain at $h = 0.3$ deep in the antiferromagnetic phase at anisotropy $\Delta = -4.5$. The eigenstates segregate cleanly into flat bands labeled by the number of domain walls W , highlighting the quasi-conserved nature of W in the deep antiferromagnetic phase. Notably, the one-meson ($W=2$) band sits at $C_j^{zz}(|\psi\rangle, |\psi_0\rangle) \simeq +4$, reflecting exactly two aligned bonds (two kinks). (b) $\langle\sigma_i^z\rangle_{\text{stag}}$ for the same parameters follows the same band pattern, further validating the domain-wall identification. (c) The von Neumann entanglement entropy S^{vN} exhibits a corresponding banded structure: low-lying $W = 2$ mesons have markedly reduced entanglement compared to the chaotic background.

The staggered magnetization $\langle\sigma_i^z\rangle_{\text{stag}}$ follows the same band pattern, reinforcing the domain-wall labeling and the emergence of an approximate conservation of W in the confined regime.

Taken together, these observations establish the following coherent picture. At small $|\Delta|$ the spectrum conforms to ETH expectations, with a Page-like dome centered at mid-spectrum. As $|\Delta|$ is made more negative, confinement suppresses entanglement and reorganizes the spectrum into correlation and entanglement bands labeled by W , signaling non-ergodic behavior. This behavior is fully consistent with the level statistics and correlation function results, establishing a coherent picture of confinement and the formation of meson-like excitations in the staggered-field XXZ chain and sets the stage for the quantitative meson spectroscopy in Sec. VI.

VI. CONTINUUM THRESHOLD, CONFINEMENT, AND ANALYTIC MESON SPECTRUM

This section will be divided into two parts. The first part will work out the analytic meson spectrum according to Rutkevich [50] while the second part will compare Rutkevich’s theory to our numerical ED results for the meson spectrum.

A. Analytic meson ladder

Rutkevich formulates the theory on the (effectively) infinite XXZ spin chain [50], and also gives a finite- N version with periodic boundary conditions for even N . The meson classification and dispersion relations are then derived in the thermodynamic limit [51]. In our comparisons below we keep the analytic (thermodynamic-limit) expressions but confront them with exact diagonalization data at finite size in the symmetry sector $(S_{\text{total}}^z, P, \mathcal{I}, \mathcal{C}_{\text{flip}}) = (0, 0, +1, +1)$. Moreover, we point out that Rutkevich’s original formulas are written

with a $J/2$ in the Hamiltonian [50]. Throughout this section we consistently adopt our J -convention used in our ED study by replacing $J/2 \mapsto J$ in the microscopic Hamiltonian. We stress that due to the existence of the staggered field the microscopic translation symmetry is by two sites (see Section II B). Consequently the total lattice momentum is defined modulo π , and we adopt $P \in [0, \pi)$ throughout. Later our ED comparisons will focus on $P = 0$.

In the staggered-field XXZ chain, neutral excitations can be viewed as pairs of domain walls, i.e. “spinons”. For fixed total momentum P , if the two spinons carry momenta $P/2 \pm p$ with single-spinon dispersion $\omega(q)$, their total energy is

$$\epsilon(p|P) = \omega(P/2 + p) + \omega(P/2 - p). \quad (6.1)$$

Here $\omega(q)$ denotes the single-spinon dispersion at $h = 0$ in the antiferromagnetic phase, and p is the *relative* momentum while P is the *total* momentum. We parameterize the two spinons by

$$\begin{aligned} p_1 &= P/2 + p \\ p_2 &= P/2 - p \end{aligned} \quad (6.2)$$

so that $\epsilon(p|P) = \omega(p_1) + \omega(p_2)$ as in Eq. (6.1). In our elliptic parametrization (see Appendix B), and in our J -convention, the single-spinon dispersion can be written in the compact form

$$\omega(q) = I \sqrt{1 - k^2 \cos^2 q}, \quad (6.3)$$

with

$$I = \frac{4J K(k) \sinh \eta}{\pi} \quad (6.4)$$

and k fixed by

$$\frac{K(k')}{K(k)} = \frac{\eta}{\pi} \quad (6.5)$$

where K is the elliptic integral and $k' = \sqrt{1 - k^2}$. Further

$$\Delta = -\cosh \eta \quad (6.6)$$

where $\eta > 0$ is the anisotropy parameter.

Varying the relative momentum p sweeps a two-spinon continuum. In the regime relevant here, $\omega(q)$ is even and convex near its minimum, so the reference threshold of the deconfined ($h = 0$) problem is obtained at $p = 0$:

$$\begin{aligned} E_{\text{cont}}(P) &= \min_p \epsilon(p|P) = \epsilon(0|P) \\ &= 2\omega(P/2). \end{aligned} \quad (6.7)$$

Using the elliptic parametrization outlined above and summarized in Appendix B, this becomes

$$E_{\text{cont}}(P) = 2I \sqrt{1 - k^2 \cos^2\left(\frac{P}{2}\right)}. \quad (6.8)$$

A staggered magnetic field confines the two spinons via a linear potential with string tension

$$f = 2h\bar{\sigma}(\eta) \quad (6.9)$$

where

$$\bar{\sigma}(\eta) = \prod_{n=1}^{\infty} \left(\frac{1 - e^{-2n\eta}}{1 + e^{-2n\eta}} \right)^2 = \prod_{n=1}^{\infty} \tanh^2(n\eta). \quad (6.10)$$

This confinement produces a discrete set of meson-like bound states, i.e. confined two-kink states. Near the deconfined threshold $E_{\text{cont}}(P)$ the relative motion reduces to an Airy quantization problem, yielding the asymptotic meson ladder

$$E_n^{(\pm)}(P) = E_{\text{cont}}(P) + A(P)z_n + f a_{\pm}(P) + \mathcal{O}(f^{4/3}), \quad (6.11)$$

with

$$A(P) = f^{2/3} \left[\frac{\epsilon''(0|P)}{2} \right]^{1/3} \quad (6.12)$$

and

$$\epsilon''(0|P) = \left. \frac{\partial^2 \epsilon(p|P)}{\partial p^2} \right|_{p=0}, \quad (6.13)$$

and where $z_n > 0$ are the magnitudes of the Airy zeros, defined by $\text{Ai}(-z_n) = 0$ for $n = 1, 2, \dots$. The $a_{\pm}(P)$ are channel-dependent $\mathcal{O}(1)$ shifts fixed by the short-distance exchange phase of the kinks (see Appendix B).

In the symmetry sector probed by our ED data, i.e. $(S_{\text{total}}^z, P, \mathcal{I}, \mathcal{C}_{\text{flip}}) = (0, 0, +1, +1)$, we compare to the even “+”-branch. For $P = 0$ one finds the closed forms

$$\begin{aligned} a_+(0) &= -\frac{\gamma_E}{\pi} \\ a_-(0) &= -\frac{\gamma_E + 2 \ln 2}{\pi} \end{aligned} \quad (6.14)$$

with

$$\gamma_E = \lim_{n \rightarrow \infty} \left(\sum_{k=1}^n \frac{1}{k} - \ln n \right) \approx 0.57722. \quad (6.15)$$

Equation (6.11) follows the Rutkevich [50]/Fonseca-Zamolodchikov [52] “positive Airy magnitudes” convention where the Airy term appears with a *plus* sign multiplying the *positive* magnitudes z_n . In this convention $E_{\text{cont}}(P)$ serves as the deconfined ($h = 0$) reference energy, and the meson tower sits *above* this reference by an amount controlled by $A(P)z_n$ plus a small channel shift given by $f a_{\pm}$. An entirely equivalent writing replaces $z_n > 0$ by the negative roots $\zeta_n < 0$ of $\text{Ai}(\zeta)$ (i.e. $\zeta_n = -z_n$), in which case the Airy correction is written as $A\zeta_n$ with $\zeta_n < 0$. We adopt the magnitude convention (6.11) throughout, because it is convenient for numerical fits of E_n versus z_n .

Two immediate corollaries are useful for data analysis. From (6.11), the near-threshold level spacings are

$$\begin{aligned} \Delta E_n(P) &\equiv E_{n+1}^{(+)}(P) - E_n^{(+)}(P) \\ &\simeq A(P) [z_{n+1} - z_n], \end{aligned} \quad (6.16)$$

which decrease slowly with n because the Airy zeros spread sublinearly. For comparison to ED, it is often convenient to subtract the n -independent offset $E_{\text{ref}}(P) \equiv E_{\text{cont}}(P) + f a_+(P)$ and analyze

$$E_n^{(+)}(P) - E_{\text{ref}}(P) \simeq A(P)z_n, \quad (6.17)$$

which yields a straight-line fit of E_n versus z_n with slope $A(P)$ and intercept fixed by E_{ref} .

At $h > 0$ the deconfined two-spinon continuum is removed and one-meson states are stable until they cross the *lightest* two-meson channel at the same total momentum. For a given P , momentum conservation assigns momenta Q and $P - Q$ to the two mesons. Since the $n = 1$ branch is the lightest meson, the lowest two-meson threshold is

$$E_{\text{th}}^{(2M)}(P) = \min_Q \left\{ E_1^{(+)}(Q) + E_1^{(+)}(P - Q) \right\}. \quad (6.18)$$

Using the near-threshold form (6.11), a one-meson level in the “+”-channel is $E_n^{(+)}(P)$. Thus, the n -th level $E_n^{(+)}(P)$ is *stable* provided that

$$\begin{aligned} E_n^{(+)}(P) &< E_{\text{th}}^{(2M)}(P) \\ \iff z_n &< \frac{E_{\text{th}}^{(2M)}(P) - E_{\text{cont}}(P) - f a_+(P)}{A(P)}. \end{aligned} \quad (6.19)$$

Since z_n grows monotonically with n , the number of stable one-meson levels at momentum P is

$$\begin{aligned} n_{\text{th}}^*(P) &= \\ \max \left\{ n : z_n &< \frac{E_{\text{th}}^{(2M)}(P) - E_{\text{cont}}(P) - f a_+(P)}{A(P)} \right\}. \end{aligned} \quad (6.20)$$

At $P=0$, the minimization in Eq. (6.18) reduces to $Q = 0$ for a symmetric dispersion. In the binding reference $b_n \equiv E_n - E_{\text{cont}}(0)$ (to be used in Fig. 6(b)),

$$b_{\text{th}}^{(2M)}(0) = E_{\text{cont}}(0) + 2[A(0)z_1 + f a_+(0)] \quad (6.21)$$

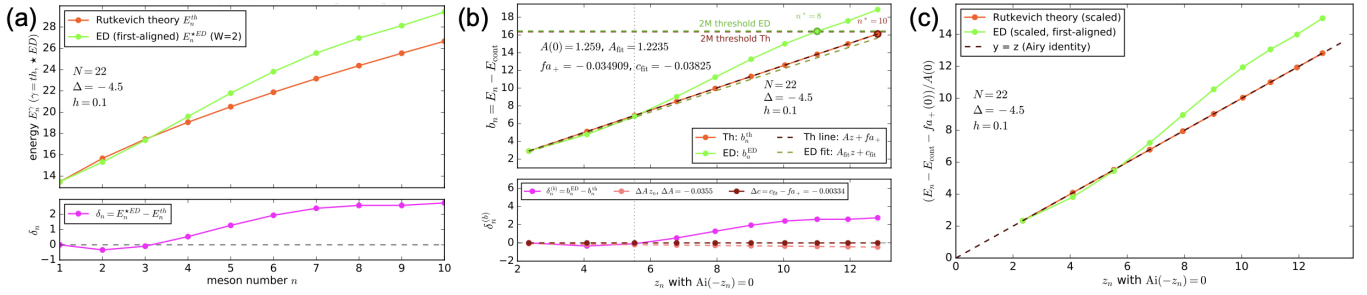


FIG. 6. *ED vs analytic $W = 2$ meson spectrum at $P = 0$ for $N = 22$, $\Delta = -4.5$, $h = 0.1$.* (a) Aligned absolute energies: ED levels E_n^{*ED} are shifted by a single constant so that $n=1$ matches theory, then compared level by level (bottom: residual δ_n). (b) Continuum–relative binding energies $b_n \equiv E_n - E_{\text{cont}}(0)$ from ED and theory vs. the Airy magnitudes z_n . Theory (solid) is the parameter-free line $A(0)z_n + f a_+(0)$ while ED (points) with linear fit $A_{\text{fit}}z_n + c_{\text{fit}}$ (dashed); fit parameters determined by the lowest three z_n points. Two horizontal 2M thresholds at $P=0$ are overlaid in the same binding reference: theory $b_{\text{th}}^{(2M)}(0) = E_{\text{cont}} + 2[A(0)z_1 + f a_+(0)]$ and ED $b_{\text{ED}}^{(2M)}(0) = E_{\text{min}}^{W=4} - E_{\text{cont}}(0)$ (lowest $W=4$ level, same symmetry sector, with the same global alignment as in panel (a)). They nearly coincide. Read-off counts are $n_{\text{th}}^* = 10$ (theory), $n_{\text{ED}}^* = 8$ (ED) since the ED $W=2$ states with $n = 9, 10$ lie just above the ED 2M line (near-threshold resonances). Bottom: residual $\delta_n^{(b)} = b_n^{\text{ED}} - b_n^{\text{th}}$ and its slope/intercept decomposition. Generally the residual $\delta_n^{(b)}$ grows with increasing z_n . (c) Airy scaling: $(E - E_{\text{cont}} - f a_+)/A$ vs. z_n ; theory lies on $y=z$ by construction, ED points collapse onto the same line for low n and start to deviate for larger n .

and

$$n_{\text{th}}^*(0) = \max\{n : b_n < b_{\text{th}}^{(2M)}(0)\} \quad (6.22)$$

with z_1 being the first Airy magnitude. Since $A(P) \propto f^{2/3}$, the right-hand side scales as $f^{-2/3}$ for weak confinement, so $n_{\text{th}}^*(P)$ increases as $h \rightarrow 0$, i.e. many shallow levels crowd near the deconfined threshold.

For a fully ED-anchored line on the same panel we take the lowest $W = 4$ level in the same symmetry sector at $P = 0$ and convert to bindings:

$$b_{\text{ED}}^{(2M)}(0) = E_{\text{min}}^{W=4} - E_{\text{cont}}(0) \quad (6.23)$$

and

$$n_{\text{ED}}^*(0) = \max\{n : b_n < b_{\text{ED}}^{(2M)}(0)\}. \quad (6.24)$$

Thus, the stability counts $n_{\text{th}}^*(0)$ can be read off against $b_{\text{th}}^{(2M)}(0)$.

In the next Section [VIB](#) we implement these criteria at $P = 0$ by plotting the bindings $b_n \equiv E_n - E_{\text{cont}}(0)$ versus the Airy magnitudes z_n , overlaying a horizontal two-meson threshold derived from Eq. (6.18), and reading off the bound–state count $n^*(P)$ via Eqs. (6.21)–(6.24). In Fig. 6(b) we draw both $b_{\text{th}}^{(2M)}(0)$ and $b_{\text{ED}}^{(2M)}(0)$ in the same binding reference $b_n \equiv E_n - E_{\text{cont}}(0)$. Thus, no approximation is taken—Eqs. (6.21)–(6.24) are used as written.

B. Numerical comparison to the analytic meson ladder at zero momentum $P = 0$

We now confront the analytic meson ladder at $P = 0$ with exact diagonalization data in the $(S_{\text{total}}^z, P, \mathcal{I}, \mathcal{C}_{\text{flip}}) = (0, 0, +1, +1)$ sector, restricted to the $W = 2$ (one-meson)

manifold. We will analyze a system consisting of $N = 22$ spins with anisotropy factor $\Delta = -4.5$ and $h = 0.1$. Additional comparisons at other field strengths h (fixed N and Δ) are presented in [Appendix C](#). For each parameter set we compute the continuum edge

$$E_{\text{cont}}(0) = 2\omega(0) = 2I\sqrt{1 - k^2}, \quad (6.25)$$

and the near-threshold ladder $E_n^{(+)}(0)$ [see Eq. (6.11)] with z_n the positive Airy magnitudes ($\text{Ai}(-z_n) = 0$) and $a_+(0) = -\gamma_E/\pi$. We analyze four standard diagnostics that emphasize complementary aspects of the ED–theory agreement.

We start with the aligned absolute meson energies depicted in Fig. 6(a) and compare absolute meson energies after a single constant alignment, i.e. the ED series is shifted so that the first ED level ($n = 1$) coincides with the analytic value. This removes an immaterial overall offset and reveals level-by-level agreement. For the lowest few levels the series nearly coincide while deviations increase gently with n , consistent with finite-size effects and subleading $\mathcal{O}(f^{4/3})$ corrections.

Next we scrutinize the binding energies [53] shown in Fig. 6(b), defined by subtracting the edge: $b_n \equiv E_n - E_{\text{cont}}(0)$. The parameter-free prediction $b_n^{\text{th}} = A(0)z_n + f a_+(0)$ is shown together with a linear regression of the ED bindings $b_n^{\text{ED}} \approx A_{\text{fit}}z_n + c_{\text{fit}}$ (fit performed versus the Airy magnitudes z_n over the indicated low-lying window $n \leq 3$). The lower panel displays the binding residual

$$\begin{aligned} \delta_n^{(b)} &\equiv b_n^{\text{ED}} - b_n^{\text{th}} \\ &= (A_{\text{fit}} - A(0))z_n + (c_{\text{fit}} - f a_+(0)) \end{aligned} \quad (6.26)$$

decomposed into “slope” and “intercept” contributions to identify the source of any mismatch. Restricting the fit window to the lowest three levels n explains the very good agreement between b_n^{th} and b_n^{ED} at small n and the larger drift for mesons with $n \geq 4$. The extracted parameters ($A_{\text{fit}}, c_{\text{fit}}$) differ modestly from the parameter-free ($A(0), f a_+(0)$), and the

residuals split into comparable slope and intercept parts over the fitted levels [see Fig. 6(b)]. Numerically, $b_{\text{th}}^{(2M)}(0)$ and $b_{\text{ED}}^{(2M)}(0)$ are nearly coincident at our parameters, reflecting that both are referenced to $b_n \equiv E_n - E_{\text{cont}}(0)$ and that the $W=4$ lowest level tracks the analytic $2M$ edge closely at $P=0$.

Crucially, we overlay two horizontal two-meson ($2M$) thresholds at $P=0$ in the *same* binding reference $b_n = E_n - E_{\text{cont}}(0)$: (i) the theory threshold $b_{\text{th}}^{(2M)}(0)$ from Eq. (6.21), and (ii) the ED threshold $b_{\text{ED}}^{(2M)}(0)$ from Eq. (6.23), obtained by taking the lowest $W=4$ level $E_{\text{min}}^{W=4}$ (same symmetry sector), applying the same global alignment as in panel (a), and subtracting $E_{\text{cont}}(0)$. The two dashed lines *2M Threshold Th* and *2M Threshold ED* in Fig. 6(b) nearly coincide. Reading off Eqs. (6.19)–(6.24), the analytic ladder yields $n_{\text{th}}^* = 10$, i.e. the $n=10$ meson energy point still lies very slightly below $b_{\text{th}}^{(2M)}(0)$. By contrast, the ED count is $n_{\text{ED}}^* = 8$ since the two mesons with $n=9$ and $n=10$ have their respective $W=2$ ED energy levels lie just *above* $b_{\text{ED}}^{(2M)}(0)$ and should be regarded as near-threshold resonances that can hybridize with the $W=4$ sector. The small difference in n^* (10 vs. 8 from theory and ED analysis, respectively) is consistent with finite-size two-meson interactions and momentum quantization in ED, together with the asymptotic (weak-confinement) nature of the theory threshold.

Now we turn our attention to the Airy scaling identity from Eq. (6.17) shown in Fig. 6(c). At $P=0$ the near-threshold analytic ladder obeys the offset-removed scaling

$$\begin{aligned} Y_n &\equiv \frac{E_n - E_{\text{cont}}(0) - f a_+(0)}{A(0)} \\ &= z_n + O(f^{4/3}), \end{aligned} \quad (6.27)$$

so that plotting Y_n against the Airy magnitudes z_n collapses the theory points exactly onto the line $Y=z$ (up to subleading $O(f^{4/3})$ corrections). Figure 6(c) displays this collapse: the ED data, after the same offset removal, fall on the same straight line for the lowest few n -levels, directly confirming the Airy quantization at $P=0$. Small systematic deviations at larger n reflect finite-size and higher-order corrections beyond the leading near-threshold form.

Finally, Fig. 7 visualizes the level spacings from Eq. (6.16). We compare the raw level spacings $\Delta E_n \equiv E_{n+1} - E_n$ between ED and analytics with theory following $A(0)[z_{n+1} - z_n]$ plotted versus the meson level index n (the underlying abscissa is the monotone sequence $z_{n+1} - z_n$). Since E_{cont} and $f a_+$ cancel in differences, spacings test only the slope $A(0)$. Agreement is best for small n and drifts gradually as n increases, in line with the residual trends above.

Additional field values h and system sizes are analyzed in Appendix C using the same protocol. The extracted $(A_{\text{fit}}, c_{\text{fit}})$ and the bound-state count n^* follow the trends anticipated from Eqs. (6.16)–(6.24).

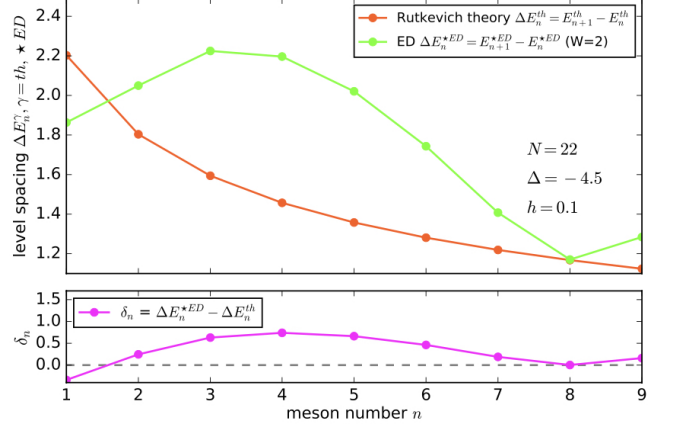


FIG. 7. Level spacings at $P=0$ for $N=22$, $\Delta = -4.5$, $h=0.1$. Top: Raw spacings $\Delta E_n^\gamma \equiv E_{n+1}^\gamma - E_n^\gamma$ for the analytic ladder theory ($\gamma=\text{th}$) and ED ($\gamma=\star \text{ED}$, $W=2$). Theory obeys the Airy-gap relation $\Delta E_n^{\text{th}} \simeq A(0)[z_{n+1} - z_n]$ [see Eq. (6.16)]. Agreement is best for the lowest few n , with gradual drift at larger n consistent with finite-size effects and subleading $O(f^{4/3})$ corrections. Bottom: spacing residual $\delta_n \equiv \Delta E_n^{\star \text{ED}} - \Delta E_n^{\text{th}}$.

VII. CONCLUSIONS

We have developed and tested a coherent confinement phenomenology for the spin- $\frac{1}{2}$ XXZ chain in a staggered magnetic field. Using exact diagonalization in symmetry-resolved sectors together with controlled near-threshold analytics, we established a consistent picture that links global spectral statistics, simple correlation diagnostics, eigenstate entanglement, and quantitative meson spectroscopy.

On the spectral side, we identified a size-dependent crossover in level statistics from GOE-like behavior at small $|\Delta|$ to nonergodic, Poisson-like statistics deep in the anti-ferromagnetic Ising regime. In real space, a single nearest-neighbor correlator organizes the spectrum into flat branches approximately labeled by the domain-wall number W . The same banding is mirrored in the eigenstate entanglement, which evolves from a Page-like dome near mid-spectrum at small $|\Delta|$ to sub-Page bands in the confined regime. The $W=2$ (one-meson) band is particularly clean, showing sharply reduced entanglement and a robust correlation plateau.

A central result is the quantitative comparison between the analytic meson ladder and ED at zero total momentum $P=0$. Near the two-spinon threshold the spectrum obeys the Airy ladder

$$E_n^{(+)}(0) = E_{\text{cont}}(0) + A(0) z_n + f a_+(0) + O(f^{4/3}),$$

with excellent agreement for the low-lying levels, consistent spacings, and an offset-removed collapse onto $y=z$. The inferred two-meson threshold yields a near-threshold counting $n^* \sim f^{-2/3}$, and small deviations are attributable to finite size and higher-order corrections.

Beyond these concrete benchmarks, our results tie directly to the broader themes of Hilbert-space fragmentation

and quantum many-body scars. In the confined regime, the emergent quasi-conservation of the domain-wall number W furnishes a *dynamical* weak-fragmentation structure, i.e. the Hilbert space is effectively partitioned into long-lived subspaces (the W -bands) that weakly hybridize on large timescales. Within these bands, we find atypical, low-entanglement eigenstates—especially in the one-meson sector—that are *scar-like* in the sense that they coexist with an otherwise chaotic background, exhibit suppressed entanglement, and organize into a simple, analytically controlled ladder. Thus, confinement provides a generic microscopic route to weak fragmentation and scar phenomenology in a disorder-free, materials-relevant model, complementary to algebraically protected examples such as PXP and AKLT families.

The same ingredients that operate here, i.e. Ising-like anisotropy and an effective staggered field, naturally arise in several quasi-one-dimensional magnets. Our correlation/entanglement banding and meson spectroscopy offer concrete, portable diagnostics: (i) finite-energy “banding” in local correlators that track W , (ii) sub-Page entanglement plateaus aligned with those bands, and (iii) near-threshold Airy spectroscopy with a field-tunable scale $A \propto f^{2/3}$. These predictions suggest targeted probes (inelastic neutron scattering near the two-spinon edge, quench dynamics from domain-wall initial states, pump-probe protocols) to look for confinement-induced weak fragmentation and scar-like response.

Our analysis is intentionally conservative, focusing on the cleanest sector ($W=2$, $P=0$) and chain lengths accessible to ED. Natural extensions include (i) a systematic study of the meson count and thresholds versus field h and momentum P , (ii) higher- W sectors to map how band hybridization sets in, (iii) dynamical signatures (revivals and slow relaxation) from specially prepared initial states, and (iv) generalizations to ladders and weakly coupled chains. Together, these directions would complete the bridge from confinement physics to fragmentation and scar phenomenology, and sharpen experimental strategies in materials where staggered fields and strong Ising anisotropy are already established.

In summary, the staggered-field XXZ chain provides a minimal, microscopically transparent platform where confinement simultaneously produces (a) a drift toward nonergodic level statistics, (b) correlation and entanglement banding labeled by the domain-wall number W , and (c) a quantitatively accurate meson ladder near threshold. Viewing the confined regime through the lens of weak fragmentation and scar formation unifies these diagnostics and clarifies why the nonergodic structure here is both robust and experimentally relevant.

VIII. ACKNOWLEDGEMENTS

JW was supported by Office of Basic Energy Sciences, Material Sciences and Engineering Division, U.S. Department of Energy (DOE) under Contracts No. DE-SC0012704. JW acknowledges the hospitality of the Perimeter Institute for Theoretical Physics as a Simons Emmy Noether Fellow, during

which part of this work was completed. Research at Perimeter Institute is supported by the Government of Canada through the Department of Innovation, Science and Economic Development Canada and by the Province of Ontario through the Ministry of Colleges and Universities.

Appendix A: \mathcal{Z}_2 symmetry for the XXZ Hamiltonian in a staggered field

We work with periodic boundary conditions and index sites as $i = 0, 1, \dots, N-1 \pmod{N}$. Because of the staggered pattern $(-1)^i$, we assume N even throughout. Define the one-site translation \mathcal{T}_1 , the two-site translation $\mathcal{T}_2 \equiv \mathcal{T}_1^2$, and the global spin flip

$$\mathcal{X} \equiv \prod_{j=0}^{N-1} \sigma_j^x \quad (\text{A1})$$

with

$$\begin{aligned} \mathcal{X} \sigma^x \mathcal{X} &= \sigma^x \\ \mathcal{X} \sigma^{y,z} \mathcal{X} &= -\sigma^{y,z}. \end{aligned} \quad (\text{A2})$$

We fix the operator ordering to

$$\mathcal{C}_{\text{flip}} \equiv \mathcal{T}_1 \mathcal{X} \quad (\text{A3})$$

which is the convention used in the main text.

The XXZ Hamiltonian in a staggered field,

$$\mathcal{H} = \mathcal{H}_J + \mathcal{H}_h, \quad (\text{A4})$$

with

$$\begin{aligned} \mathcal{H}_J &= -J \sum_{i=0}^{N-1} \left(\sigma_i^x \sigma_{i+1}^x + \sigma_i^y \sigma_{i+1}^y + \Delta \sigma_i^z \sigma_{i+1}^z \right) \\ \mathcal{H}_h &= -h \sum_{i=0}^{N-1} (-1)^i \sigma_i^z, \end{aligned} \quad (\text{A5})$$

is invariant under $\mathcal{C}_{\text{flip}}$, and $\mathcal{C}_{\text{flip}}$ squares to a two-site translation:

$$\mathcal{C}_{\text{flip}} \mathcal{H} \mathcal{C}_{\text{flip}}^{-1} = \mathcal{H}, \quad \mathcal{C}_{\text{flip}}^2 = \mathcal{T}_2. \quad (\text{A6})$$

To make progress we now prove the invariance of the field term. Using $\mathcal{T}_1 \sigma_i^z \mathcal{T}_1^{-1} = \sigma_{i+1}^z$ and $\mathcal{X} \sigma_i^z \mathcal{X} = -\sigma_i^z$, we have

$$\begin{aligned} \mathcal{C}_{\text{flip}} \sigma_i^z \mathcal{C}_{\text{flip}}^{-1} &= \mathcal{T}_1 \mathcal{X} \sigma_i^z \mathcal{X} \mathcal{T}_1^{-1} = \mathcal{T}_1 (-\sigma_i^z) \mathcal{T}_1^{-1} \\ &= -\sigma_{i+1}^z. \end{aligned} \quad (\text{A7})$$

Hence

$$\begin{aligned} \mathcal{C}_{\text{flip}} \mathcal{H}_h \mathcal{C}_{\text{flip}}^{-1} &= -h \sum_i (-1)^i (-\sigma_{i+1}^z) \\ &= -h \sum_j (-1)^{j-1} \sigma_j^z \\ &= -h \sum_j (-1)^j \sigma_j^z \\ &= \mathcal{H}_h, \end{aligned} \quad (\text{A8})$$

where in the last step we used $(-1)^{j-1} = -(-1)^j$ and the overall minus sign cancels the explicit minus from conjugation.

Now we prove the invariance of the exchange term. First, \mathcal{T}_1 permutes bonds, so $\mathcal{T}_1 \mathcal{H}_J \mathcal{T}_1^{-1} = \mathcal{H}_J$. Second, \mathcal{X} flips the sign of each $\sigma^{y,z}$ but leaves σ^x invariant. Therefore for every bond term

$$\begin{aligned} \mathcal{X}(\sigma_i^\alpha \sigma_{i+1}^\alpha) \mathcal{X} &= (\mathcal{X} \sigma_i^\alpha \mathcal{X}) (\mathcal{X} \sigma_{i+1}^\alpha \mathcal{X}) \\ &= (\pm \sigma_i^\alpha) (\pm \sigma_{i+1}^\alpha) \\ &= \sigma_i^\alpha \sigma_{i+1}^\alpha \end{aligned} \quad (\text{A9})$$

with $\alpha = x, y, z$ and $\mathcal{X} \mathcal{H}_J \mathcal{X} = \mathcal{H}_J$. Thus $\mathcal{C}_{\text{flip}} \mathcal{H}_J \mathcal{C}_{\text{flip}}^{-1} = \mathcal{H}_J$, completing the proof of $\mathcal{C}_{\text{flip}} \mathcal{H} \mathcal{C}_{\text{flip}}^{-1} = \mathcal{H}$.

We remark that with the ordering (A3),

$$\begin{aligned} \mathcal{C}_{\text{flip}}^2 &= \mathcal{T}_1 \mathcal{X} \mathcal{T}_1 \mathcal{X} = \mathcal{T}_1 (\mathcal{T}_1 \mathcal{X}') \mathcal{X} = \mathcal{T}_2 \mathcal{X}' \mathcal{X} \\ &= \mathcal{T}_2, \end{aligned} \quad (\text{A10})$$

where $\mathcal{X}' \equiv \mathcal{T}_1 \mathcal{X} \mathcal{T}_1^{-1} = \prod_j \sigma_{j+1}^x$ (each σ_j^x is shifted by one site). Since $\mathcal{X}' \mathcal{X} = \prod_j \sigma_{j+1}^x \prod_j \sigma_j^x = \mathbf{1}$ (every site appears exactly once), Eq. (A10) follows. Hence $\mathcal{C}_{\text{flip}}$ is a square root of \mathcal{T}_2 .

Since $\mathcal{C}_{\text{flip}}$ commutes with \mathcal{H} and $\mathcal{C}_{\text{flip}}^2 = \mathcal{T}_2$, each two-site momentum sector of \mathcal{T}_2 ,

$$P_n = \frac{4\pi n}{N}, \quad n = 0, 1, \dots, \frac{N}{2} - 1, \quad (\text{A11})$$

decomposes into two subsectors labeled by the eigenvalue $C_f = \pm 1$ of $\mathcal{C}_{\text{flip}}$. This is the symmetry resolution used in our ED calculations.

Appendix B: Analytic Description of Meson Energies

This Appendix records the working formulas used in Sec. VI in a compact, self-contained way and in the *same* sign convention we use in the main text (Rutkevich [50]/Fonseca-Zamolodchikov [52]): the Airy magnitudes $z_n > 0$ are defined by $\text{Ai}(-z_n) = 0$, and the near-threshold correction appears with a plus sign. Again we stress that Rutkevich's original formulas are written with a factor of $J/2$ in the Hamiltonian [50]. Throughout this section we consistently adopt our J -convention used in ED by replacing $J/2 \mapsto J$ in the microscopic Hamiltonian.

Throughout Appendix B we consider an infinite (thermodynamic) chain when writing the analytic two-kink kinematics: the total momentum P labels the center-of-mass motion while p denotes the relative momentum, so that

$$\epsilon(p|P) = \omega\left(\frac{P}{2} + p\right) + \omega\left(\frac{P}{2} - p\right). \quad (\text{B1})$$

The continuum threshold at fixed P is thus $E_{\text{cont}}(P) = 2\omega(P/2)$ obtained by minimizing $\epsilon(p|P)$ at $p = 0$. In the ED comparisons of Sec. VI we work at finite length N (typically $N = 20, 22$) and total two-site momentum $P = 0$ and finite-size effects enter only through subleading corrections to the near-threshold ladder.

B.1 One-kink dispersion and two-kink kinematics

The first ingredient is the dispersion of the one-kink states, $\omega(p)$. These energies are

$$\omega(p) = I [1 - k^2 \cos^2(p)]^{1/2} \quad (\text{B2})$$

with

$$I = \frac{4JK(k) \sinh(\eta)}{\pi} \quad (\text{B3})$$

where η is a parameterization of the anisotropy of the spin chain, i.e. $\Delta = -\cosh(\eta)$, and $K(k)$ is the elliptic integral with modulus k fixed by the relation

$$\frac{K(\sqrt{1-k^2})}{K(k)} = \frac{\eta}{\pi}. \quad (\text{B4})$$

The energies of two kink states with total momentum P in the absence of the staggered field are given by

$$\epsilon(p|P) = \omega(P/2 + p) + \omega(P/2 - p). \quad (\text{B5})$$

The lower boundary of the two-kink continuum at fixed total momentum P is obtained by minimizing $\epsilon(p|P)$ at $p = 0$, which gives

$$E_{\text{cont}}(P) = 2\omega\left(\frac{P}{2}\right) = 2I \sqrt{1 - k^2 \cos^2\left(\frac{P}{2}\right)} \quad (\text{B6})$$

with $I = 4JK(k) \sinh \eta / \pi$ in our J -convention and k fixed by $K(k')/K(k) = \eta/\pi$. In particular, at $P = 0$ one has $E_{\text{cont}}(0) = 2I\sqrt{1-k^2}$.

B.2 Scattering phases and meson energies

We are going to be focused on mesons in the total spin $S_{\text{total}}^z = 0$ sector. There are two such types of mesons which are distinguished by the action of the modified translation operator \tilde{T}_1 defined in Ref. [50]:

$$\tilde{T}_1 |\text{meson}, s = 0, \pm\rangle = \pm |\text{meson}, s = 0, \pm\rangle, \quad (\text{B7})$$

where we distinguished the two types of mesons with the labels \pm . The scattering phases that govern the interchange of the two kinks in the two-kink state equal

$$\theta_{\pm}(\alpha) = \theta_0(\alpha) + \chi_{\pm}(\alpha) \quad (\text{B8})$$

with

$$\begin{aligned} \theta_0(\alpha) &= \alpha + \sum_{n=1}^{\infty} \frac{e^{-n\eta} \sin(2\alpha n)}{n \cosh(n\eta)} \\ \chi_+ &= -i \ln \left(-\frac{\sin[(\alpha + i\eta)/2]}{\sin[(\alpha - i\eta)/2]} \right) \\ \chi_- &= -i \ln \left(-\frac{\cos[(\alpha + i\eta)/2]}{\cos[(\alpha - i\eta)/2]} \right). \end{aligned} \quad (\text{B9})$$

The energies of the confined two-kink states are indexed by the integer n and are given in terms of these phases, i.e.

$$E_{\text{meson}}(n, \pm, P) = \epsilon(0, P) + A(P) z_n + f a_{\pm}(P) \quad (\text{B10})$$

with the ‘‘Airy scale’’

$$A(P) = f^{2/3} \left(\frac{\partial_p^2 \epsilon(p, P)|_{p=0}}{2} \right) \quad (\text{B11})$$

and

$$a_{\pm}(P) = \frac{-2J \sinh(\eta)}{\omega(P/2)} \partial_{\alpha} \theta_{\pm}(\alpha) \Big|_{\alpha=0}. \quad (\text{B12})$$

Here $-z_n < 0$ is the n -th zero of the Airy function along the negative real axis. We follow the positive-magnitude convention for Airy zeros, writing $z_n > 0$ such that $\text{Ai}(-z_n) = 0$, so the near-threshold correction appears as $+A(P) z_n$. (Equivalently, one may use the negative zeros $\zeta_n < 0$ with $\text{Ai}(\zeta_n) = 0$, in which case $z_n = -\zeta_n$ and the formula is unchanged after the substitution $z_n \mapsto -\zeta_n$.)

The so-called string tension $f = 2h\bar{\sigma}(\eta)$ contains the spontaneous magnetization $\bar{\sigma}(\eta)$ that is defined by

$$\bar{\sigma}(\eta) = \prod_{n=1}^{\infty} \left(\frac{1 - e^{-2\eta n}}{1 + e^{-2\eta n}} \right)^2 = \prod_{n=1}^{\infty} \tanh^2(\eta n) \quad (\text{B13})$$

so that $A(P) = f^{2/3} [e''(0|P)/2]^{1/3}$.

At $P = 0$ we compare continuum-relative bindings $b_n \equiv E_n - E_{\text{cont}}(0)$, which to leading orders obey

$$b_n = A(0) z_n + f a_+(0) + O(f^{4/3}). \quad (\text{B14})$$

Linear fits of b_n^{ED} versus z_n extract $(A_{\text{fit}}, c_{\text{fit}})$ for comparison with the parameter-free $(A(0), f a_+(0))$.

B.3 Airy scale and curvature

For the second derivative contained in the ‘‘Airy scale’’ (B11) we determine

$$\begin{aligned} \epsilon''(0|P) &= \frac{\partial^2}{\partial p^2} [\omega(P/2+p) + \omega(P/2-p)] \Big|_{p=0} \\ &= 2\omega''\left(\frac{P}{2}\right). \end{aligned} \quad (\text{B15})$$

With $\omega(q)$ from (B2), we arrive at the following expression

$$\omega''(q) = 2I \left[\frac{k^2 \cos 2q}{\sqrt{1 - k^2 \cos^2 q}} - \frac{k^4 \cos^2 q \sin^2 q}{(1 - k^2 \cos^2 q)^{3/2}} \right] \quad (\text{B16})$$

which simplifies for $P = 0$ to

$$\epsilon''(0|0) = \frac{4I k^2}{\sqrt{1 - k^2}}. \quad (\text{B17})$$

We also list the derivatives of the expressions (B8) and (B9) with respect to the variable α as

$$\begin{aligned} \frac{\partial}{\partial \alpha} \theta_0(\alpha) \Big|_{\alpha=0} &= \left[1 + 2 \sum_{n=1}^{\infty} \frac{e^{-n\eta} \cos(2\alpha n)}{\cosh(n\eta)} \right] \Big|_{\alpha=0} \\ &= 1 + 2 \sum_{n=1}^{\infty} \frac{e^{-n\eta}}{\cosh(n\eta)} \\ \chi'_+(\alpha) \Big|_{\alpha=0} &= -\frac{i}{2} \left[\cot\left(\frac{\alpha + i\eta}{2}\right) - \cot\left(\frac{\alpha - i\eta}{2}\right) \right] \Big|_{\alpha=0} \\ &= -\coth\left(\frac{\eta}{2}\right) \\ \chi'_-(\alpha) \Big|_{\alpha=0} &= -\frac{i}{2} \left[-\tan\left(\frac{\alpha + i\eta}{2}\right) + \tan\left(\frac{\alpha - i\eta}{2}\right) \right] \Big|_{\alpha=0} \\ &= -\tanh\left(\frac{\eta}{2}\right) \end{aligned} \quad (\text{B18})$$

utilizing the identities $\cot(ix) = -i \coth(x)$ and $\tan(ix) = i \tanh(ix)$ at $\alpha = 0$. Thus, the χ_{\pm} -parts contribute the compact, real values

$$\begin{aligned} \chi'_+(0) &= -\coth(\eta/2) \\ \chi'_-(0) &= -\tanh(\eta/2). \end{aligned} \quad (\text{B19})$$

The ‘‘bulk’’ series gives the expression listed in (B18) for $\theta'_0(0)$ which by itself is not convergent. It is designed to cancel the large- n pieces implicit in $\chi'_{\pm}(0)$. Resumming with standard θ -function/digamma identities produces a finite $\theta'_{\pm}(0)$. Finally we arrive at the following expression for the coefficients $a_{\pm}(P)$:

$$\begin{aligned} a_{\pm}(P) &= -\frac{2J \sinh(\eta)}{\omega(P/2)} \theta'_{\pm}(0) \\ &= -\frac{\pi}{2K(k)\sqrt{1 - k^2 \cos^2(P/2)}} \theta'_{\pm}(0). \end{aligned} \quad (\text{B20})$$

Upon working in the zero momentum sector $P = 0$ the residual η -dependence cancels and you arrive at the universal constants

$$\begin{aligned} a_+(0) &= -\frac{\gamma_E}{\pi} \\ a_-(0) &= -\frac{\gamma_E + 2 \ln 2}{\pi}. \end{aligned} \quad (\text{B21})$$

with

$$\gamma_E = \lim_{n \rightarrow \infty} \left(\sum_{k=1}^n \frac{1}{k} - \ln n \right). \quad (\text{B22})$$

The constant γ_E is the Euler-Mascheroni constant with an approximate value of $\gamma_E \approx 0.5772156649$. These values are used in Sec. VI when comparing with ED at $P = 0$.

B.4 Evaluation of $a_{\pm}(P)$ at $P = 0$

In order to evaluate $a_{\pm}(P)$ for zero momentum $P = 0$ we briefly collect the relevant definitions [54]:

$$\omega(p) = I\sqrt{1 - k^2 \cos^2 p} \quad (\text{B23})$$

$$I = \frac{4J K(k) \sinh \eta}{\pi} \quad (\text{B24})$$

$$a_{\pm}(P) = -\frac{2J \sinh \eta}{\omega(P/2)} \left. \frac{\partial \theta_{\pm}(\alpha)}{\partial \alpha} \right|_{\alpha=0} \quad (\text{B25})$$

$$\theta_{\pm}(\alpha) = \theta_0(\alpha) + \chi_{\pm}(\alpha) \quad (\text{B26})$$

with

$$\theta_0(\alpha) = \alpha + \sum_{n=1}^{\infty} \frac{e^{-n\eta}}{n \cosh(n\eta)} \sin(2n\alpha) \quad (\text{B27})$$

$$\chi_+(\alpha) = -i \ln \left(\frac{-\sin[(\alpha + i\eta)/2]}{\sin[\alpha - i\eta]/2} \right) \quad (\text{B28})$$

$$\chi_-(\alpha) = -i \ln \left(\frac{-\cos[(\alpha + i\eta)/2]}{\cos[(\alpha - i\eta)/2]} \right). \quad (\text{B29})$$

To make progress we divide this subsection into five *Steps 1-5*.

Step 1: explicit α -derivative of the χ_{\pm} pieces. Using

$$\frac{d}{d\alpha} \ln \sin \frac{\alpha \pm i\eta}{2} = \frac{1}{2} \cot \frac{\alpha \pm i\eta}{2} \quad (\text{B30})$$

$$\frac{d}{d\alpha} \ln \cos \frac{\alpha \pm i\eta}{2} = -\frac{1}{2} \tan \frac{\alpha \pm i\eta}{2},$$

we obtain

$$\chi'_+(\alpha) = -\frac{i}{2} \left[\cot \frac{\alpha + i\eta}{2} - \cot \frac{\alpha - i\eta}{2} \right] \quad (\text{B31})$$

$$\chi'_-(\alpha) = -\frac{i}{2} \left[-\tan \frac{\alpha + i\eta}{2} + \tan \frac{\alpha - i\eta}{2} \right]. \quad (\text{B32})$$

Utilizing the identities $\cot(ix) = -i \coth x$ and $\tan(ix) = i \tanh x$ leads to

$$\boxed{\chi'_+(0) = -\coth \frac{\eta}{2}, \quad \chi'_-(0) = -\tanh \frac{\eta}{2}}. \quad (\text{B33})$$

for $\alpha = 0$.

Step 2: α -derivative of the bulk series at $\alpha = 0$. From (B27),

$$\theta'_0(0) = 1 + 2 \sum_{n=1}^{\infty} \frac{e^{-n\eta}}{\cosh(n\eta)}. \quad (\text{B34})$$

Introduce the nome $q \equiv e^{-\eta} \in (0, 1)$. Noting $\frac{e^{-n\eta}}{\cosh(n\eta)} =$

$$\frac{2}{1 + e^{-2n\eta}} = \frac{2}{1 + q^{2n}},$$

$$\boxed{\theta'_0(0) = 1 + 4 \sum_{n=1}^{\infty} \frac{1}{1 + q^{2n}}}. \quad (\text{B35})$$

Step 3: combine $\theta'_0(0)$ with $\chi'_{\pm}(0)$. Using the classical expansions

$$\begin{aligned} \coth \frac{\eta}{2} &= 1 + 2 \sum_{n=1}^{\infty} \frac{q^n}{1 - q^n} \\ \tanh \frac{\eta}{2} &= 1 - 2 \sum_{n=1}^{\infty} \frac{q^n}{1 + q^n}, \end{aligned} \quad (\text{B36})$$

and (B33)–(B35), we obtain the convergent combinations

$$\begin{aligned} \theta'_+(0) &= \theta'_0(0) + \chi'_+(0) \\ &= \left[1 + 4 \sum_{n=1}^{\infty} \frac{1}{1 + q^{2n}} \right] - \left[1 + 2 \sum_{n=1}^{\infty} \frac{q^n}{1 - q^n} \right] \\ &= 4 \sum_{n=1}^{\infty} \frac{1}{1 + q^{2n}} - 2 \sum_{n=1}^{\infty} \frac{q^n}{1 - q^n}, \end{aligned} \quad (\text{B37})$$

and

$$\begin{aligned} \theta'_-(0) &= \theta'_0(0) + \chi'_-(0) \\ &= \left[1 + 4 \sum_{n=1}^{\infty} \frac{1}{1 + q^{2n}} \right] - \left[1 - 2 \sum_{n=1}^{\infty} \frac{q^n}{1 + q^n} \right] \\ &= 4 \sum_{n=1}^{\infty} \frac{1}{1 + q^{2n}} + 2 \sum_{n=1}^{\infty} \frac{q^n}{1 + q^n}. \end{aligned} \quad (\text{B38})$$

The apparent divergences have cancelled between θ'_0 and χ'_{\pm} and both series are absolutely convergent for $q \in (0, 1)$.

Step 4: short resummation via theta/digamma identities at $P = 0$. At zero momentum $P = 0$ the prefactor in (B25) simplifies, using (B23),

$$-\frac{2J \sinh \eta}{\omega(0)} = -\frac{2J \sinh \eta}{I\sqrt{1 - k^2}} = -\frac{\pi}{2K(k)\sqrt{1 - k^2}}. \quad (\text{B39})$$

It is convenient to express the q -series in (B37)–(B38) in terms of Jacobi theta functions $\theta_j(0|q)$ and the Dedekind eta function $\eta(q)$ via their infinite products [55–57]. After taking logarithms and differentiating with respect to $\ln q$ (and using the elliptic relation $q = e^{-\eta} = e^{-\pi K'(k)/K(k)}$ [55, 58]), one finds that the combinations appearing in (B37)–(B38) can be rewritten as

$$\begin{aligned} \frac{\pi}{2K(k)\sqrt{1 - k^2}} \theta'_+(0) &= \frac{\gamma_E}{\pi} \\ \frac{\pi}{2K(k)\sqrt{1 - k^2}} \theta'_-(0) &= \frac{\gamma_E - 2 \ln 2}{\pi}, \end{aligned} \quad (\text{B40})$$

where γ_E is the Euler–Mascheroni constant. A direct route is to pass through the logarithmic derivatives of the product representations for $\theta_2(0|q)$, $\theta_4(0|q)$ and $\eta(q)$, and then use the classical digamma identities $\psi(1) = -\gamma_E$ and $\psi(\frac{1}{2}) = -\gamma_E - 2 \ln 2$, together with duplication/reflection formulas to collapse the q -series to the constants on the right-hand side of (B40) [55, 57, 59].

Step 5: final result for $a_{\pm}(0)$. Inserting (B39) and (B40) into (B25) at $P = 0$ gives

$$a_{\pm}(0) = -\frac{2J \sinh \eta}{\omega(0)} \theta'_{\pm}(0) = -\frac{\pi}{2K(k)\sqrt{1-k^2}} \theta'_{\pm}(0)$$

$$\Rightarrow \boxed{a_+(0) = -\frac{\gamma_E}{\pi}, \quad a_-(0) = \frac{-\gamma_E + 2 \ln 2}{\pi}}. \quad (\text{B41})$$

Note that the constants $a_{\pm}(0)$ are *universal*, i.e. they are independent of J , η and k , as the J -dependence cancels in (B39) and the residual η - and k -dependence cancels in (B40). We stress that the only place where the J -normalization matters is in the prefactors of (B24) and (B25).

Additional information: explicit product/derivative identities used in Step 4. Set the nome $q \equiv e^{-\eta} \in (0, 1)$ and recall the q -Pochhammer symbol $(a; q)_{\infty} := \prod_{n=0}^{\infty} (1 - a q^n)$ [60]. We will also use the Jacobi theta functions at $z = 0$ and the Dedekind eta function in product form (with our real nome q):

$$\eta(q) = q^{1/24} (q; q)_{\infty}, \quad (\text{B42})$$

$$\theta_2(0|q) = 2 q^{1/4} (q^2; q^2)_{\infty} (-q; q^2)_{\infty}^2, \quad (\text{B43})$$

$$\theta_4(0|q) = (q^2; q^2)_{\infty} (q; q^2)_{\infty}^2, \quad (\text{B44})$$

where $(q; q^2)_{\infty} = \prod_{n \geq 1} (1 - q^{2n-1})$ and $(-q; q^2)_{\infty} = \prod_{n \geq 1} (1 + q^{2n-1})$. These product representations are standard; see, e.g., [55–57].

Auxiliary t -derivatives (to avoid n -weights). For t near 1, define the auxiliary products

$$F_-(t) := (t; q)_{\infty} = \prod_{n \geq 1} (1 - t q^n)$$

$$G_+(t) := (-t; q)_{\infty} = \prod_{n \geq 1} (1 + t q^n) \quad (\text{B45})$$

$$H_+(t) := (-t; q^2)_{\infty} = \prod_{n \geq 1} (1 + t q^{2n}).$$

Then differentiation with respect to $\ln t$ produces the *unweighted* basic series:

$$\left. \frac{\partial}{\partial \ln t} \ln F_-(t) \right|_{t=1} = -\sum_{n \geq 1} \frac{q^n}{1 - q^n}, \quad (\text{B46})$$

$$\left. \frac{\partial}{\partial \ln t} \ln G_+(t) \right|_{t=1} = \sum_{n \geq 1} \frac{q^n}{1 + q^n}, \quad (\text{B47})$$

$$\left. \frac{\partial}{\partial \ln t} \ln H_+(t) \right|_{t=1} = \sum_{n \geq 1} \frac{q^{2n}}{1 + q^{2n}}. \quad (\text{B48})$$

Moreover,

$$\frac{1}{1 + q^{2n}} = 1 - \frac{q^{2n}}{1 + q^{2n}}$$

$$\Rightarrow \sum_{n \geq 1} \frac{1}{1 + q^{2n}} = \sum_{n \geq 1} 1 - \left. \frac{\partial}{\partial \ln t} \ln H_+(t) \right|_{t=1} \quad (\text{B49})$$

and the divergent constant $\sum_{n \geq 1} 1$ cancels out when inserted into the combinations (B37)–(B38).

Rewriting the convergent combinations. Using (B46)–(B48) in (B37)–(B38) yields

$$\theta'_+(0) = -4 \left. \frac{\partial}{\partial \ln t} \ln H_+(t) \right|_{t=1} - 2 \left. \frac{\partial}{\partial \ln t} \ln F_-(t) \right|_{t=1} + (\text{cancelling constant}) \quad (\text{B50})$$

$$\theta'_-(0) = 4 \sum_{n \geq 1} \frac{1}{1 + q^{2n}} + 2 \left. \frac{\partial}{\partial \ln t} \ln G_+(t) \right|_{t=1}. \quad (\text{B51})$$

The first line (B50) is already in terms of H_+ and F_- . For the second line (B51), introduce also

$$\widehat{H}_+(t) := (-t; q^2)_{\infty}, \quad \widehat{G}_+(t) := (-t; q)_{\infty},$$

so that $\partial_{\ln t} \ln \widehat{H}_+(t)|_{t=1}$ and $\partial_{\ln t} \ln \widehat{G}_+(t)|_{t=1}$ reproduce the two series in (B51) via (B48)–(B47).

Passage to θ/η via infinite products. From (B43)–(B44) and (B42) one finds (up to explicit powers of q , which drop out after $\partial_{\ln t}$ at $t = 1$) that

$$\begin{aligned} \theta_4(0|q) &\propto (q^2; q^2)_{\infty} (q; q^2)_{\infty}^2 \\ \theta_2(0|q) &\propto (q^2; q^2)_{\infty} (-q; q^2)_{\infty}^2 \\ \eta(q) &\propto (q; q)_{\infty}. \end{aligned} \quad (\text{B52})$$

A short algebraic rearrangement shows that the *finite* combinations (B50)–(B51) can be written as logarithmic derivatives (with respect to $\ln q$) of these modular objects [56]; equivalently,

$$\frac{\pi}{2K(k)\sqrt{1-k^2}} \theta'_+(0) = -\frac{\partial}{\partial \ln q} \left[\ln (\theta_4(0|q) \eta(q)) \right], \quad (\text{B53})$$

$$\frac{\pi}{2K(k)\sqrt{1-k^2}} \theta'_-(0) = -\frac{\partial}{\partial \ln q} \left[\ln (\theta_2(0|q) \eta(q)) \right]. \quad (\text{B54})$$

Here we have also used the standard elliptic identities at $z = 0$, $\frac{2K(k)}{\pi} = \theta_3(0|q)^2$ and $\sqrt{1-k^2} = \theta_4(0|q)^2/\theta_3(0|q)^2$, to normalize the left-hand sides [55, 58].

Evaluation via Γ/ψ . Employing the infinite-product representations of $\theta_2(0|q)$, $\theta_4(0|q)$ and $\eta(q)$, then differentiating w.r.t. $\ln q$ and invoking the duplication and reflection formulas for the digamma function $\psi = \Gamma'/\Gamma$ (together with the special values $\psi(1) = -\gamma_E$ and $\psi(\frac{1}{2}) = -\gamma_E - 2 \ln 2$) [55, 57, 59], one obtains the *constants*

$$\begin{aligned} \frac{\pi}{2K(k)\sqrt{1-k^2}} \theta'_+(0) &= \frac{\gamma_E}{\pi} \\ \frac{\pi}{2K(k)\sqrt{1-k^2}} \theta'_-(0) &= \frac{\gamma_E - 2 \ln 2}{\pi}, \end{aligned} \quad (\text{B55})$$

which are precisely (B40).

Combining this with the $P = 0$ prefactor (B39) in our convention,

$$\begin{aligned} a_{\pm}(0) &= -\frac{2J \sinh \eta}{\omega(0)} \theta'_{\pm}(0) \\ &= -\frac{\pi}{2K(k)\sqrt{1-k^2}} \theta'_{\pm}(0), \end{aligned} \quad (\text{B56})$$

we conclude

$$\boxed{a_+(0) = -\frac{\gamma_E}{\pi}, \quad a_-(0) = \frac{-\gamma_E + 2 \ln 2}{\pi}}.$$

To summarize the procedure we remark that the evaluation at $P = 0$ proceeds by writing $\theta_{\pm}(\alpha) = \theta_0(\alpha) \pm \chi_{\pm}(\alpha)$, differentiating at $\alpha = 0$, and then using the product/eta/theta identities listed below to resum the large- n pieces in $\theta'_0(0)$ against those implicit in $\chi'_{\pm}(0)$. This yields $(\frac{\pi}{2K\sqrt{1-k^2}})\theta'_+(0) = \gamma_E/\pi$ and $(\frac{\pi}{2K\sqrt{1-k^2}})\theta'_-(0) = (\gamma_E - 2 \ln 2)/\pi$, hence $a_+(0) = -\gamma_E/\pi$ and $a_-(0) = (-\gamma_E + 2 \ln 2)/\pi$ in our J -convention.

B.5 Identities used to evaluate $\theta'_{\pm}(0)$

We collect here the minimal formulas invoked in Section B.4.

Nome, modulus, and complete elliptic integral. With $q = e^{-2\eta}$,

$$k = \frac{\vartheta_2^2(0|q)}{\vartheta_3^2(0|q)}, \quad k' = \frac{\vartheta_4^2(0|q)}{\vartheta_3^2(0|q)}, \quad K(k) = \frac{\pi}{2} \vartheta_3^2(0|q).$$

Dedekind eta and Jacobi theta (product forms).

$$\begin{aligned} \eta_D(q) &= q^{1/24} \prod_{n \geq 1} (1 - q^n) \\ \vartheta_2(0|q) &= 2q^{1/4} \prod_{n \geq 1} (1 - q^n)(1 + q^n)^2 \\ \vartheta_3(0|q) &= \prod_{n \geq 1} (1 - q^n) (1 + q^{n-\frac{1}{2}})^2 \\ \vartheta_4(0|q) &= \prod_{n \geq 1} (1 - q^n) (1 - q^{n-\frac{1}{2}})^2 \end{aligned} \quad (\text{B57})$$

and $\vartheta'_1(0|q) = 2q^{1/4} \prod_{n \geq 1} (1 - q^n)^3$, with $\ln \vartheta_1(\alpha|q) = \ln \vartheta'_1(0|q) + \ln \alpha + O(\alpha^2)$ as $\alpha \rightarrow 0$.

Logarithmic-derivative trick. Using the even/odd product splits, the finite combinations obtained in Section B.4 can be written as

$$\begin{aligned} \frac{\pi}{2K(k)\sqrt{1-k^2}} \theta'_+(0) &= -\frac{\partial}{\partial \ln q} \ln \left[\frac{\vartheta_4(0|q)}{\eta_D(q)} \right] \\ \frac{\pi}{2K(k)\sqrt{1-k^2}} \theta'_-(0) &= -\frac{\partial}{\partial \ln q} \ln \left[\frac{\vartheta_2(0|q)}{\eta_D(q)} \right]. \end{aligned} \quad (\text{B58})$$

Digamma special values. With $\psi = \Gamma'/\Gamma$,

$$\psi(1) = -\gamma_E, \quad \psi\left(\frac{1}{2}\right) = -\gamma_E - 2 \ln 2.$$

These produce the constants quoted in Eqs. (B55)–(B56) and, hence, $a_{\pm}(0)$.

B.6 Airy zeros and spacings

Let $z_n > 0$ be the magnitudes defined by $\text{Ai}(-z_n) = 0$ ($n=1, 2, \dots$). The large- n asymptotics

$$z_n = \left[\frac{3\pi}{2} \left(n - \frac{1}{4} \right) \right]^{2/3} [1 + \mathcal{O}(n^{-2})] \quad (\text{B59})$$

is useful for initialization. Near threshold, level spacings follow

$$\begin{aligned} \Delta E_n(P) &= E_{n+1}^{(+)}(P) - E_n^{(+)}(P) \\ &\simeq A(P) [z_{n+1} - z_n]. \end{aligned} \quad (\text{B60})$$

Appendix C: Additional numerical data

This Appendix collects supplementary ED results that complement the main text. We present (i) additional level-statistics data across anisotropy Δ at several staggered fields h and system sizes $N = 18, 20, 22$, and (ii) further comparisons between the analytic meson ladder and ED at zero total momentum $P = 0$ for fields different from those shown in the main text. The goal is twofold: to document the robustness of the chaos–nonergodicity crossover in spectral statistics and to illustrate how the near-threshold meson spectroscopy behaves as h is varied at fixed (N, Δ) .

C.1 Level-spacing ratios at additional staggered fields h

Figure 8 summarizes the mean adjacent-gap ratio $\langle r \rangle$ versus anisotropy Δ in the symmetry sector $(S_{\text{total}}^z, P, \mathcal{I}, \mathcal{C}_{\text{flip}}) = (0, 0, +1, +1)$ for several chain lengths $N = 18, 20, 22$ and staggered fields $h = 0.1, 0.2, 0.4$. As in Section III, $\langle r \rangle$ serves as a sensitive, unfolding-free diagnostic of spectral correlations, with the Gaussian-orthogonal-ensemble (GOE) value $\langle r \rangle_{\text{GOE}} \approx 0.536$ indicating quantum chaos and the Poisson value $\langle r \rangle_{\text{Poisson}} \approx 0.386$ indicating integrable/uncorrelated statistics.

Figure 8 (a) presents results for the case of $h = 0.1$. A clear size dependence is visible already at moderate anisotropy. For $N = 18$ and $N = 20$, the mean ratio $\langle r \rangle$ lies noticeably below the GOE benchmark $\langle r \rangle_{\text{GOE}} \approx 0.536$ once $\Delta \lesssim -1.5$, indicating an early drift away from fully chaotic statistics. By contrast, $N = 22$ remains close to the GOE value over the same range of Δ , with a departure that sets in only at more negative anisotropy. As Δ is decreased further into the AF

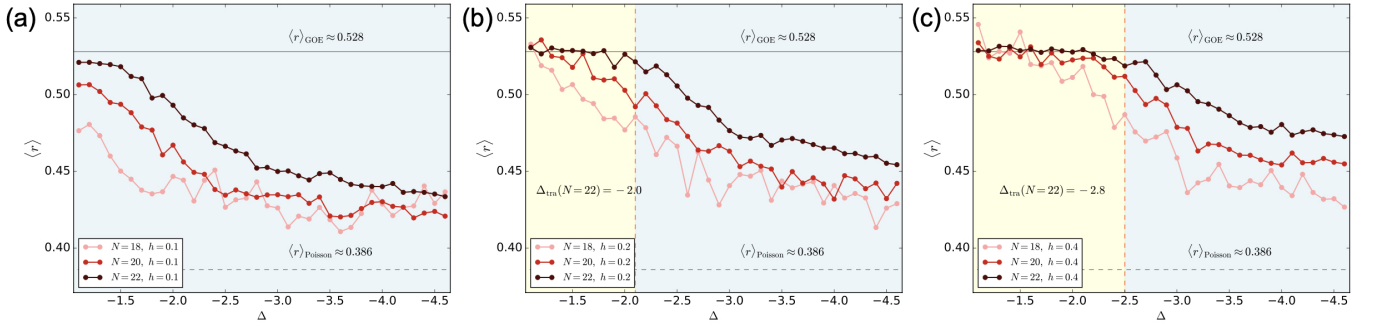


FIG. 8. Level-spacing ratios $\langle r \rangle$ for the spin- $\frac{1}{2}$ XXZ chain ($J=1$) across anisotropy Δ at several staggered fields h . Mean adjacent-gap ratio $\langle r \rangle$ in the sector $(S_{\text{total}}^z, P, \mathcal{I}, \mathcal{C}_{\text{flip}}) = (0, 0, +1, +1)$ for chain lengths $N = 18, 20, 22$ at (a) $h=0.1$, (b) $h=0.2$, (c) $h=0.4$. Horizontal lines mark the GOE benchmark $\langle r \rangle_{\text{GOE}} \approx 0.528$ and the Poisson value $\langle r \rangle_{\text{Poisson}} \approx 0.386$. (a) For $h=0.1$, all sizes lie below the GOE line over the full range of Δ , with $N=22$ closest—consistent with finite-size suppression that weakens as N increases. (b) For $h=0.2$, a GOE-like plateau is visible at small $|\Delta|$. For $N = 22$ it persists up to $\Delta \gtrsim -2.0$ (yellow shaded area), whereas smaller N depart earlier. As Δ is made more negative, $\langle r \rangle$ drifts toward Poisson (blue shaded area). The crossover shifts to more negative Δ with increasing N . (c) For $h=0.4$, the same pattern holds with the crossover further displaced, i.e. the $N = 22$ curve remains GOE-like up to $\Delta \gtrsim -2.8$ (yellow shaded area) before trending downward. Overall, increasing h moves the GOE \rightarrow nonergodic crossover to more negative Δ , modulating—but not reversing—the trends. This aligns with the confinement-induced banding seen in correlations and entanglement (Secs. IV and V).

Ising regime, all sizes N trend downward toward Poisson-like values $\langle r \rangle_{\text{Poisson}} \approx 0.386$, with the crossover shifted to more negative Δ for larger N —consistent with the finite-size trend discussed in the main text.

A pronounced size dependence remains in Figure 8(b) presenting the case of $h = 0.2$. For $N = 18$, finite-size effects are sizable: $\langle r \rangle$ already sits well below the GOE benchmark at relatively small $|\Delta|$, indicating an early departure from fully chaotic statistics. For $N = 20$ and $N = 22$, these effects are much weaker. In particular, the $N = 22$ curve stays at GOE-like values up to about $|\Delta| \lesssim 2.1$ (i.e., $\Delta \gtrsim -2.1$) before exhibiting a clear downturn. As in panel (a), the crossover shifts to more negative Δ with increasing system size.

For the case $h = 0.4$ shown in Figure 8(c) we see that for very small $|\Delta|$, all sizes $N = 18, 20, 22$ lie essentially on the GOE benchmark, confirming fully chaotic statistics in this regime. As $|\Delta|$ increases, the curves separate, i.e. the smaller the system, the earlier $\langle r \rangle$ departs from the GOE value and begins its downward drift. For the largest size available ($N = 22$) the GOE plateau persists up to roughly $\Delta \approx -2.5$, beyond which a clear crossover toward non-GOE values sets in. At more negative Δ , all sizes continue to trend downward toward Poisson-like statistics, consistent with confinement-induced nonergodicity. Across all panels (a)-(c), these field-resolved trends dovetail with the correlation/entanglement “banding” discussed in Secs. IV-V: as confinement strengthens at large negative Δ , eigenstates segregate by domain-wall number W , level repulsion weakens across bands, and $\langle r \rangle$ correspondingly falls below GOE.

Overall, Fig. 8 provides a global view consistent with the main text: (i) a GOE-like regime at modest $|\Delta|$; (ii) a size-dependent crossover toward nonergodic statistics deep in the AF Ising phase; and (iii) a mild field dependence that modulates, but does not invert, these trends.

C.2 Additional information for the numerical comparison to the analytic meson ladder at zero momentum $P = 0$

Here we repeat the $P = 0$ meson spectroscopy of Sec. VI for the same system size and anisotropy, $(N, \Delta) = (22, -4.5)$, at two additional staggered fields h : a weaker field $h = 0.05$ (closer to the deconfined limit) and a stronger field $h = 0.2$. For each h we display the same diagnostics as in Fig. 6 of the main text: (i) aligned absolute energies (a single global shift so that the $n = 1$ meson coincides), (ii) continuum–relative bindings $b_n \equiv E_n - E_{\text{cont}}(0)$ versus Airy magnitudes z_n , overlaid with the parameter-free theory line $A(0)z_n + f a_+(0)$ and an ED fit $A_{\text{fit}}z_n + c_{\text{fit}}$, together with the two–meson thresholds drawn in the same binding reference, and (iii) the Airy scaling collapse $(E - E_{\text{cont}} - f a_+)/A$ versus z_n . Together these panels illustrate how changing h affects the Airy slope $A(0) \propto f^{2/3}$ and the constant term $f a_+(0)$, and how the low-lying ED mesons track the parameter-free analytic ladder as long as finite-size and subleading $O(f^{4/3})$ corrections remain small. For completeness we also include the raw level-spacing plots $\Delta E_n \equiv E_{n+1} - E_n$ in the style of Fig. 7.

At $h = 0.05$ (see Fig. 9), the Airy scale $A(0) \propto f^{2/3}$ is reduced, the ladder is denser near threshold, and the ED bindings track the parameter-free line over a wider range of n than at $h = 0.1$. The two–meson threshold in binding units sits higher relative to the low-lying levels, so more $W = 2$ states lie below it, consistent with the trend $n^* \sim f^{-2/3}$ from Eqs. (6.19)–(6.20). The offset-removed collapse $(E - E_{\text{cont}} - f a_+)/A \rightarrow z$ holds cleanly for the lowest several levels, while residuals grow gently with n , in line with finite-size and subleading $O(f^{4/3})$ corrections.

At $h = 0.2$ (Fig. 10), stronger confinement steepens the ladder and reduces the number of bound $W = 2$ states below the two–meson line. Agreement between ED and the parameter-free theory remains very good at the lowest n , with earlier

departures as n increases. The residual decomposition indicates a slightly larger slope mismatch compared to smaller h , whereas the intercept remains close to $f a_+(0)$.

The level-spacing panels depicted in Fig. 11 make the slope trend explicit: since E_{cont} and $f a_+$ cancel in differences,

$\Delta E_n^{\text{th}} \simeq A(0)[z_{n+1} - z_n]$ directly probes $A(0)$. Spacings are overall smaller at $h = 0.05$ and larger at $h = 0.2$, with the closest ED-theory agreement near threshold in both cases and a mild, systematic drift at larger n .

-
- [1] J. M. Deutsch, Quantum statistical mechanics in a closed system, *Phys. Rev. A* **43**, 2046 (1991).
- [2] M. Srednicki, Chaos and quantum thermalization, *Phys. Rev. E* **50**, 888 (1994).
- [3] D. M. Basko, I. L. Aleiner, and B. L. Altshuler, Metal-insulator transition in a weakly interacting many-electron system with localized single-particle states, *Annals of Physics* **321**, 1126 (2006).
- [4] R. Nandkishore and D. A. Huse, Many-body localization and thermalization in quantum statistical mechanics, *Annual Review of Condensed Matter Physics* **6**, 15 (2015).
- [5] V. Khemani, M. Hermele, and R. Nandkishore, Localization from hilbert space shattering: From theory to physical realizations, *Phys. Rev. B* **101**, 174204 (2020).
- [6] L. Zhao, P. R. Datla, W. Tian, M. M. Aliyu, and H. Loh, Observation of quantum thermalization restricted to hilbert space fragments and F_{2k} scars, *Phys. Rev. X* **15**, 011035 (2025).
- [7] P. Sala, T. Rakovszky, R. Verresen, M. Knap, and F. Pollmann, Ergodicity breaking arising from hilbert space fragmentation in dipole-conserving hamiltonians, *Phys. Rev. X* **10**, 011047 (2020).
- [8] S. Moudgalya, B. A. Bernevig, and N. Regnault, Quantum many-body scars and hilbert space fragmentation: a review of exact results, *Rep. Prog. Phys.* **85**, 086501 (2022).
- [9] Z.-C. Yang, F. Liu, A. V. Gorshkov, and T. Iadecola, Hilbert-space fragmentation from strict confinement, *Phys. Rev. Lett.* **124**, 207602 (2020).
- [10] T. Kohler, S. Scherg, P. Sala, F. Pollmann, B. H. Madhusudhana, I. Bloch, and M. Aidelsburger, Exploring the regime of fragmentation in strongly tilted fermi-hubbard chains, *Phys. Rev. Lett.* **130**, 010201 (2023).
- [11] L. Zhao, P. R. Datla, W. Tian, M. M. Aliyu, and H. Loh, Observation of quantum thermalization restricted to hilbert space fragments and $2\mathcal{K}$ scars, *Phys. Rev. X* **15**, 011035 (2025).
- [12] V. Khemani, M. Hermele, R. Nandkishore, and R. Moessner, Localization from hilbert space fragmentation, *Nature Physics* **15**, 1231 (2019).
- [13] S. Moudgalya, E. J. Bergholtz, N. Regnault, and S. L. Sondhi, Quantum many-body scars and hilbert space fragmentation: A review of exact results, *Reviews of Modern Physics* **94**, 045005 (2022).
- [14] A. Chandran and V. Khemani, Quantum many-body scars and hilbert space fragmentation: Past, present, and future, *Annual Review of Condensed Matter Physics* **14**, 443 (2023).
- [15] H. Bernien, S. Schwartz, A. Keesling, H. Levine, A. Omran, H. Pichler, S. Choi, A. S. Zibrov, M. Endres, M. Greiner, V. Vuletić, and M. D. Lukin, Probing many-body dynamics on a 51-atom quantum simulator, *Nature* **551**, 579 (2017).
- [16] D. Bluvstein, A. Omran, H. Levine, A. Keesling, G. Semeghini, T. Wang, S. Ebadi, H. Bernien, A. S. Zibrov, H. Pichler, S. Choi, J. Cui, M. Rossignolo, M. Kalinowski, J. Kolder, L.-P. Henry, A. Vishwanath, and M. D. Lukin, Controlling quantum many-body dynamics in driven rydberg atom arrays, *Science* **371**, 1355 (2021).
- [17] C. J. Turner, A. A. Michailidis, D. A. Abanin, M. Serbyn, and Z. Papić, Weak ergodicity breaking from quantum many-body scars, *Nature Physics* **14**, 745 (2018).
- [18] C. J. Turner, A. A. Michailidis, D. A. Abanin, M. Serbyn, and Z. Papić, Quantum scarred eigenstates in a rydberg atom chain: Entanglement, breakdown of thermalization, and stability to perturbations, *Phys. Rev. B* **98**, 155134 (2018).
- [19] S. Choi, C. J. Turner, H. Pichler, W. W. Ho, A. A. Michailidis, Z. Papić, M. Serbyn, M. D. Lukin, and D. A. Abanin, Emergent su(2) dynamics and perfect quantum many-body scars, *Phys. Rev. Lett.* **122**, 220603 (2019).
- [20] W. W. Ho, S. Choi, H. Pichler, and M. D. Lukin, Periodic orbits, entanglement, and quantum many-body scars in constrained models: Matrix product state approach, *Phys. Rev. Lett.* **122**, 040603 (2019).
- [21] N. Shiraishi and T. Mori, Systematic construction of counterexamples to the eigenstate thermalization hypothesis, *Physical Review Letters* **119**, 030601 (2017).
- [22] M. Schecter and T. Iadecola, Weak ergodicity breaking and quantum many-body scars in spin-1 xy magnets, *Physical Review Letters* **123**, 147201 (2019).
- [23] S. Moudgalya, S. Rachel, B. A. Bernevig, and N. Regnault, Exact excited states of nonintegrable models, *Physical Review B* **98**, 235155 (2018).
- [24] S. B. Rutkevich, Energy spectrum of bound-spinons in the quantum ising spin chain with a longitudinal magnetic field, *Journal of Statistical Mechanics: Theory and Experiment* , P07015 (2010).
- [25] A. J. A. James and R. M. Konik, Quantum dynamics of excitations in strongly confined ising spin chains, *Physical Review B* **87**, 241103 (2013).
- [26] N. J. Robinson, A. J. A. James, and R. M. Konik, Signatures of rare states and thermalization in a theory with confinement, *Phys. Rev. B* **99**, 195108 (2019).
- [27] A. J. A. James, R. M. Konik, and N. J. Robinson, Nonthermal states arising from confinement in one and two dimensions, *Phys. Rev. Lett.* **122**, 130603 (2019).
- [28] H. Kim, T. N. Ikeda, and D. A. Huse, Testing whether all eigenstates obey the eigenstate thermalization hypothesis, *Phys. Rev. E* **90**, 052105 (2014).
- [29] A. J. A. James, R. M. Konik, P. Lecheminant, N. J. Robinson, and A. M. Tsvelik, Non-perturbative methodologies for low-dimensional strongly-correlated systems: From non-abelian bosonization to truncated spectrum methods, *Reports on Progress in Physics* **81**, 046002 (2018).
- [30] S. Moudgalya, N. Regnault, and B. A. Bernevig, Exact excited states of nonintegrable models and quantum many-body scars, *Physical Review B* **98**, 235156 (2018).
- [31] I. Affleck, T. Kennedy, E. H. Lieb, and H. Tasaki, Rigorous results on valence-bond ground states in antiferromagnets, *Physical Review Letters* **59**, 799 (1987).
- [32] N. O’Dea, F. J. Burnell, A. Chandran, and V. Khemani, From quantum chaos to localization transition in the spin-1 aklt chain, *Physical Review Letters* **124**, 040605 (2020).

- [33] L. L. Kish, A. Weichselbaum, D. M. Pajerowski, A. T. Savici, A. Podlesnyak, L. Vasylechko, A. Tsvetik, R. Konik, and I. A. Zaliznyak, High-temperature quantum coherence of spinons in a rare-earth spin chain, *Nature Communications* **16**, 10.1038/s41467-025-61715-z (2025).
- [34] L. Wu, S. E. Nikitin, M. Brando, L. Vasylechko, G. Ehlers, M. Frontzek, A. T. Savici, G. Sala, A. D. Christianson, M. D. Lumsden, *et al.*, Antiferromagnetic ordering and dipolar interactions of ybalo 3, *Physical Review B* **99**, 195117 (2019).
- [35] L. Wu, S. Nikitin, Z. Wang, W. Zhu, C. D. Batista, A. Tsvetik, A. M. Samarakoon, D. A. Tennant, M. Brando, L. Vasylechko, *et al.*, Tomonaga–luttinger liquid behavior and spinon confinement in ybalo3, *Nature communications* **10**, 698 (2019).
- [36] O. Breunig, M. Garst, E. Sela, B. Buldmann, and P. e. a. Becker, The spin- $\frac{1}{2}$ xxz chain system cs_2cocl_4 in a transverse magnetic field, *Phys. Rev. Lett.* **111**, 187202 (2013).
- [37] R. Coldea, D. A. Tennant, E. M. Wheeler, E. Wawrzynska, D. Prabhakaran, M. T. F. Telling, K. Habicht, P. Smeibidl, and K. Kiefer, Quantum criticality in an ising chain: Experimental evidence for emergent e_8 symmetry, *Science* **327**, 177 (2010).
- [38] H. Zou, Y. Cui, X. Wang, Z. Zhang, J. Yang, G. Xu, A. Okutani, M. Hagiwara, M. Matsuda, G. Wang, G. Mussardo, K. Hódsági, M. Kormos, Z. He, S. Kimura, R. Yu, J. Ma, and J. Wu, E_8 spectra of quasi-one-dimensional antiferromagnet $\text{baco}_2\text{v}_2\text{o}_8$ under transverse field, *Phys. Rev. Lett.* **127**, 077201 (2021).
- [39] Z. Wang, T. Lorenz, D. I. Gorbunov, P. T. Cong, Y. Kohama, S. Niesen, O. Breunig, J. Engelmayer, A. Hermann, J. Wu, K. Kindo, J. Wosniza, S. Zherlitsyn, and A. Loidl, Quantum criticality of an ising-like spin- $\frac{1}{2}$ antiferromagnetic chain in a transverse magnetic field, *Phys. Rev. Lett.* **120**, 207205 (2018).
- [40] Q. Faure, S. Takayoshi, S. Petit, V. Simonet, S. Raymond, L.-P. Regnault, M. Boehm, J. S. White, M. Månsson, C. Rüegg, P. Lejay, B. Canals, T. Lorenz, S. C. Furuya, T. Giamarchi, and B. Grenier, Topological quantum phase transition in the ising-like antiferromagnetic spin chain $\text{baco}_2\text{v}_2\text{o}_8$, *Nature Physics* **14**, 716 (2018).
- [41] M. Matsuda, H. Onishi, A. Okutani, J. Ma, P. Agrawal, T. Hong, D. M. Pajerowski, J. R. D. Copley, K. Okunishi, M. Mori, S. Kimura, and M. Hagiwara, Magnetic structure and dispersion relation of the quasi-one-dimensional ising-like antiferromagnet $\text{baco}_2\text{v}_2\text{o}_8$ in a transverse magnetic field, *Phys. Rev. B* **96**, 024439 (2017).
- [42] S. Kimura, H. Yashiro, K. Okunishi, M. Hagiwara, Z. He, K. Kindo, T. Taniyama, and M. Itoh, Field-induced order-disorder transition in antiferromagnetic $\text{baco}_2\text{v}_2\text{o}_8$ driven by a softening of spinon excitations, *Phys. Rev. Lett.* **99**, 087602 (2007).
- [43] B. Grenier, S. Petit, V. Simonet, E. Canévet, L.-P. Regnault, S. Raymond, B. Canals, C. Berthier, and P. Lejay, Longitudinal and transverse zeeman ladders in the ising-like chain antiferromagnet $\text{baco}_2\text{v}_2\text{o}_8$, *Phys. Rev. Lett.* **114**, 017201 (2015).
- [44] A. K. Bera, B. Lake, F. H. L. Essler, L. Vanderstraeten, C. Hubig, U. Schollwöck, A. T. M. N. Islam, A. Schneidewind, and D. L. Quintero-Castro, Spinon confinement in a quasi-one-dimensional anisotropic heisenberg magnet, *Phys. Rev. B* **96**, 054423 (2017).
- [45] Z. Wang, M. Schmidt, A. K. Bera, A. T. M. N. Islam, B. Lake, A. Loidl, and J. Deisenhofer, Spinon confinement in the one-dimensional ising-like antiferromagnet $\text{srco}_2\text{v}_2\text{o}_8$, *Phys. Rev. B* **91**, 140404(R) (2015).
- [46] L. D’Alessio, Y. Kafri, A. Polkovnikov, and M. Rigol, From quantum chaos and eigenstate thermalization to statistical mechanics and thermodynamics, *Advances in Physics* **65**, 239 (2016), <https://doi.org/10.1080/00018732.2016.1198134>.
- [47] V. Oganesyan and D. A. Huse, Localization of interacting fermions at high temperature, *Phys. Rev. B* **75**, 155111 (2007).
- [48] The average longitudinal magnetization defined as Eq. (4.1) without the alternating factor $(-1)^i$ is zero since we work in the $S_{\text{total}}^z = 0$ sector.
- [49] The energy shift E_{shift} is introduced to avoid the data belonging to the different values of anisotropy Δ (partially) lying on top of each other.
- [50] S. B. Rutkevich, Spinon confinement in the gapped antiferromagnetic xxz spin- $\frac{1}{2}$ chain, *Phys. Rev. B* **106**, 134405 (2022).
- [51] For zero staggered field $h = 0$ the infinite-chain Hamiltonian is written with a $J/2$ prefactor and sums over $j \in \mathbb{Z}$; a finite- N version with PBC is also given and reduces to the same results in the $N \rightarrow \infty$ limit.
- [52] P. Fonseca and A. Zamolodchikov, Ising field theory in a magnetic field: Analytic properties of the free energy, (2001), [arXiv:hep-th/0112167](https://arxiv.org/abs/hep-th/0112167).
- [53] All thresholds and bindings in Fig. 6(b) use the same reference $E_{\text{cont}}(0)$. This avoids ambiguities when comparing ED and theory lines.
- [54] We stress that the expression are valid for our choice of coupling constant J in the Hamiltonian (2.1). Rutkevich’s convention employs a coupling constant of $J/2$ instead of J and specific expressions need to be adjusted to accommodate for that choice.
- [55] NIST Digital Library of Mathematical Functions, NIST Digital Library of Mathematical Functions, <https://dlmf.nist.gov/> (2010), online companion to the NIST Handbook of Mathematical Functions.
- [56] E. T. Whittaker and G. N. Watson, *A Course of Modern Analysis*, 4th ed. (Cambridge University Press, Cambridge, 1996) reprint of the 4th edition (1927).
- [57] M. Abramowitz and I. A. Stegun, eds., *Handbook of Mathematical Functions with Formulas, Graphs, and Mathematical Tables* (Dover, New York, 1965).
- [58] F. W. J. Olver, D. W. Lozier, R. F. Boisvert, and C. W. Clark, eds., *NIST Handbook of Mathematical Functions* (Cambridge University Press, New York, 2010).
- [59] F. W. J. Olver, *Asymptotics and Special Functions* (AK Peters, Wellesley, MA, 1997) reprint of the 1974 Academic Press edition.
- [60] G. Gasper and M. Rahman, *Basic Hypergeometric Series*, 2nd ed., *Encyclopedia of Mathematics and its Applications*, Vol. 96 (Cambridge University Press, Cambridge, 2004).

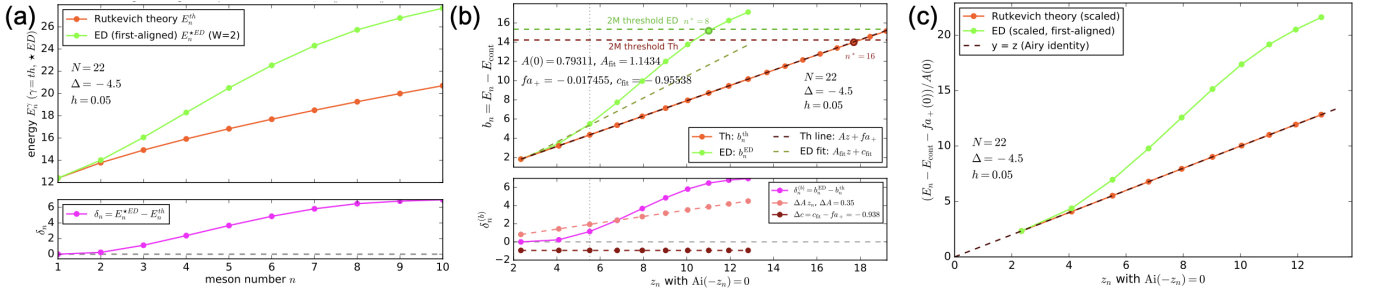


FIG. 9. *ED vs analytic $W = 2$ meson spectrum at $P = 0$ for $N = 22$, $\Delta = -4.5$, $h = 0.05$ (additional data).* (a) Aligned absolute energies: ED levels are shifted by a single constant so that the $n=1$ meson coincides with theory. Energies E_n^{*ED} are larger than the respective theory ladder energies. (b) Continuum–relative bindings $b_n \equiv E_n - E_{\text{cont}}(0)$ versus Airy magnitudes z_n : parameter–free theory line $A(0)z_n + f a_+(0)$ (solid) and ED linear fit $A_{\text{fit}}z_n + c_{\text{fit}}$ (dashed) with residual $\delta_n^{(b)} = b_n^{\text{ED}} - b_n^{\text{th}}$ and its slope/intercept decomposition. Horizontal dashed lines mark the two–meson thresholds drawn in the same binding reference: $b_{\text{th}}^{(2M)}(0) = E_{\text{cont}}(0) + 2[A(0)z_1 + f a_+(0)]$ and $b_{\text{ED}}^{(2M)}(0) = E_{\text{min}}^{W=4} - E_{\text{cont}}(0)$. The two nearly coincide. Many low-lying theory levels fall beneath them, consistent with $n_{\text{th}}^*(P)$ increasing as $h \rightarrow 0$, i.e. many shallow levels crowd near the deconfined threshold. (c) Airy scaling collapse $(E - E_{\text{cont}} - f a_+)/A$ versus z_n : the theory points lie on $y = z$ by construction and the ED points collapse onto the same line for the lowest few mesons n , with small, systematic deviations at larger levels n .

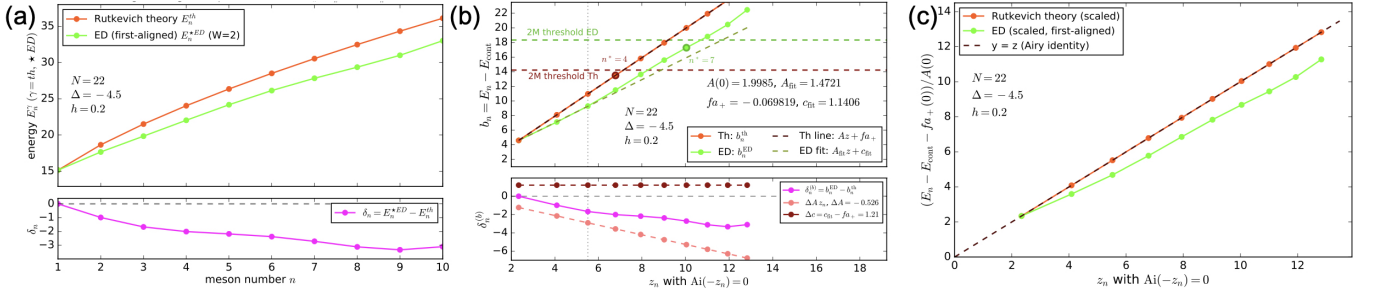


FIG. 10. *ED vs analytic $W = 2$ meson spectrum at $P = 0$ for $N = 22$, $\Delta = -4.5$, $h = 0.2$ (additional data).* Same layout as Fig. 9. (a) Aligned absolute energies: ED levels are shifted by a single constant so that the $n=1$ meson coincides with theory. The ED energy points now are smaller than the corresponding theory ladder values. (b) The larger field increases the Airy scale $A(0) \propto f^{2/3}$ and the offset $f a_+(0)$, steepening the ladder. The ED and theory $2M$ thresholds remain close. Fewer ED levels lie below the $2M$ line than at $h = 0.05$, consistent with the expected decrease of n^* as h grows. (c) The Airy collapse in again holds cleanly for the lowest few levels.

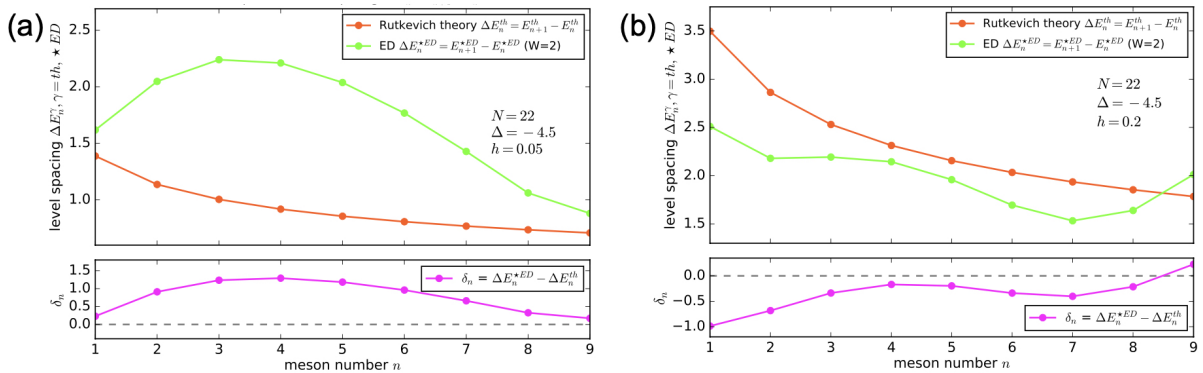


FIG. 11. *Level spacings at $P = 0$ for $N = 22$, $\Delta = -4.5$, $h = 0.05, 0.2$ (additional data).* Raw spacings $\Delta E_n \equiv E_{n+1} - E_n$ for theory and ED in the $W=2$ sector compared with the Airy prediction $\Delta E_n^{\text{th}} \simeq A(0)[z_{n+1} - z_n]$ [Eq. (6.16)]. (a) $h = 0.05$: smaller $A(0)$ yields tighter spacings and a longer near–threshold window of close ED–theory agreement. (b) $h = 0.2$: larger $A(0)$ produces larger spacings and a shorter agreement window as finite–size and $O(f^{4/3})$ effects become visible with increasing n .